Accepted Manuscript

Anatexis of former arc magmatic rocks during oceanic subduction: A case study from the north Wulan gneiss complex

Xiucai Li, Manlan Niu, Chris Yakymchuk, Zhen Yan, Changlei Fu, Qiqi Zhao

PII: S1342-937X(18)30148-5
DOI: doi:10.1016/j.gr.2018.04.016
Reference: GR 1981

To appear in: *Gondwana Research*

Received date: 12 October 2017
Revised date: 19 March 2018
Accepted date: 25 April 2018

Please cite this article as: Xiucai Li, Manlan Niu, Chris Yakymchuk, Zhen Yan, Changlei Fu, Qiqi Zhao , Anatexis of former arc magmatic rocks during oceanic subduction: A case study from the north Wulan gneiss complex. Gr (2018), doi:10.1016/j.gr.2018.04.016

Anatexis of former arc magmatic rocks during oceanic subduction: A case study from the North Wulan gneiss complex

Xiucai Li[a,b], Manlan Niu[a*], Chris Yakymchuk[b], Zhen Yan[c], Changlei Fu[c,d], Qiqi Zhao[a]

[a] School of Resources and Environmental Engineering, Hefei University of Technology, Hefei 230009, China

[b] Department of Earth and Environmental Sciences, University of Waterloo, Waterloo, ON, N2L 3G1, Canada

[c] Institute of Geology, Chinese Academy of Geological Sciences, Beijing 100037, China

[d] MLR Key Laboratory of Metallogeny and Mineral Assessment, Institute of Mineral Resources, Chinese Academy of Geological Sciences, Beijing 100037, China

*Corresponding Author: Manlan Niu

E-mail: hfnml@hfut.edu.cn

Address: School of Resources and Environmental Engineering, Hefei University of Technology, No.193, Tunxi Road, Hefei 230009, Anhui Province, China

Abstract

Migmatites are widespread in the North Wulan gneiss complex from the South Qilian–North Qaidam orogenic belt, but their petrogenesis and ages are poorly constrained. Here, an integrated study of petrography, whole-rock geochemistry, geochronology, zircon trace element and Hf isotope analysis deciphers the nature and timing of partial melting in migmatitic amphibole-biotite gneiss. Zircon U–Pb geochronology reveals that the protoliths crystallized at 506–494 Ma followed by metamorphism and anatexis at *ca.* 465 to 450 Ma. Hafnium isotope compositions of inherited cores and anatectic rims are very similar, suggesting that partial melting occurred in a relatively closed isotopic system and new zircon rims grew via dissolution–reprecipitation of pre-existing zircon cores. Anatexis occurred by water-fluxed melting of mafic-intermediate rocks through the breakdown of biotite and growth of peritectic amphibole. The protolith of the migmatites records Cambrian arc magmatism in an active continental margin, which was induced by northward subduction of the South Qilian ocean slab. Contemporary arc-like magmatism and high-temperature/low-pressure metamorphism in the region suggest that anatexis in the North Wulan gneiss complex likely took place in a continental arc setting, which reflects the reworking of former arc magmatic rocks in a late stage of oceanic subduction.

Key words Migmatite; Zircon; Water-fluxed melting; South Qilian; North Qaidam

1. Introduction

Migmatites are widespread in ancient and modern orogenic belts and are a critical link between high-grade metamorphism and regional-scale magmatism especially in continental arcs and collision zones (Whitney and Irving, 1994; Brown et al., 2010). Migmatites record anatexis and crustal reworking during high-temperature metamorphism and carry critical information about the thermomechanical evolution of the deep crust (e.g. Brown, 2007). In deep crustal settings, partial melting usually occurs through incongruent hydrate-breakdown reactions (Clemens, 2006; Brown, 2013). However, anatexis due to the influx of externally-derived hydrous fluids is an important process in some migmatite terranes (e.g. Slagstad et al., 2005; Sawyer, 2010; Weinberg and Hasalová, 2015; Hu et al., 2016). The generation, transport and final fate of crustal melts are strongly influenced by the thermal and geodynamic processes associated with orogenesis (Brown, 2001; Vanderhaeghe and Teyssier, 2001). The processes of melt formation, evolution and migration in migmatites are also crucial for understanding the chemical differentiation of the continental crust (Vielzeuf et al., 1990) as well as the formation of granitoids in the middle to shallow crust during orogenesis (Solar and Brown, 2001). Therefore, it is important to elucidate the timing and nature of anatexis in migmatite terranes of various metamorphic grades and tectonic settings.

The South Qilian–North Qaidam orogenic belt records a complete history of orogenic evolution from seafloor subduction to subsequent continental collision (Song et al., 2014a; Zhang et al., 2017). It experienced multiple early Paleozoic metamorphic events associated with partial melting (Song et al., 2014a; Zhang et al., 2017). Two mechanisms have been proposed to account for these partial melting events: decompression melting of eclogite (Song

et al., 2014b; Zhang et al., 2015; Yu et al., 2017a) and melting of the thickened lower crustal under granulite-facies conditions (Yu et al., 2012, 2014, 2017b). Migmatites in the North Wulan gneiss complex occur in the hanging wall of this subduction system and record pervasive amphibolite- to granulite-facies metamorphism, but do not contain the hallmark minerals of hydrate-breakdown melting in the granulite facies (e.g. garnet and orthopyroxene). In addition, no eclogites are present that could reflect decompression melting in this complex. A possible alternative mechanism is that widespread amphibole-biotite migmatites in the North Wulan gneiss complex may represent relatively low-temperature water-fluxed melting. Therefore, the rocks in the North Wulan gneiss complex provide an excellent opportunity to investigate different mechanisms of partial melting in the same orogenic system. In this contribution, zircon U–Pb geochronology and Lu–Hf isotope analysis are coupled with geochemistry and petrography to elucidate the mechanism and timing of partial melting in the North Wulan gneiss complex and relate this to the tectonic evolution of the South Qilian–North Qaidam orogenic belt.

2. Geological background

2.1. Regional geology

The South Qilian–North Qaidam orogenic belt is located at the NW margin of the Qinghai-Tibet plateau (Fig. 1a). It is bounded by the large sinistral strike-slip Altyn-Tagh fault to the west, merges with the West Qinling orogenic belt in the east, and is truncated by the smaller Wahongshan-Wenquan fault to the southeast. The Qilian Block and the Qaidam Block are found to the north and south of the South Qilian–North Qaidam orogenic belt, respectively

(Fig. 1b). This belt is divided into the North Qaidam high pressure to ultrahigh pressure (HP–UHP) metamorphic complex in the south, the Oulongbuluke microcontinental block in the center, and the South Qilian accretionary complex in the north. The North Qaidam HP–UHP metamorphic complex extends towards the NWW for ~400 km and contains eclogites, garnet peridotites, as well as high-pressure metagranitic and metapelitic gneisses (Yang et al., 2006; Yu et al., 2013; Song et al., 2005; 2006; 2014a; Zhang et al., 2005, 2017). The HP–UHP metamorphic complex is interpreted to have resulted from the early Paleozoic collision between the Qilian and Qaidam Blocks at 460–420 Ma (Song et al., 2006; Zhang et al., 2009; Zhang et al., 2010; Yu et al., 2013). The South Qilian accretionary complex crops out discontinuously along a NW–SE orientation for ~1000 km and is mainly comprised of Cambrian ophiolite sequences and Ordovician arc-related volcanic sequences (Fu et al., 2014; Zhang et al., 2017; Song et al., 2017). It represents the product of subduction–accretion during the closure of the South Qilian ocean (Xiao et al., 2009; Yan et al., 2015; Song et al., 2017).

The Oulongbuluke microcontinental block is one of several ancient continental blocks at the southeastern edge of Tarim Block. It is proposed to represent a remnant of a cratonic fragment detached from the Tarim Block (e.g. Lu et al., 2006; Chen et al., 2012). This microcontinental block is composed of a medium-grade to high-grade metamorphic crystalline basement and an unmetamorphosed sedimentary cover (Lu et al., 2006; Chen et al., 2009; Wang et al., 2009). The Oulongbuluke microcontinental block is separated from the South Qilian accretionary complex by the Qinghai Lake-Nanshan Fault in the north and from the North Qaidam HP–UHP metamorphic complex by the Wulan-Yuka Fault in the south (Fig. 1b). Previous studies of the Oulongbuluke microcontinental block have focused on the

assembly and breakup of the supercontinents Columbia and Rodinia (Lu et al., 2006; Chen et al., 2009; Wang et al., 2009; Wang et al., 2016; Yu et al., 2017c). However, the role that the Oulongbuluke microcontinental block played in the evolution of the Proto-Tethyan ocean is still unclear, although some researchers speculate that the Oulongbuluke microcontinental block was accreted to the north and amalgamated with the Qilian Block in the early Paleozoic on the basis of regional correlations (Xiao et al., 2009; Yan et al., 2012, 2015).

The basement of the Oulongbuluke microcontinental block consists of the early Paleoproterozoic Delingha Complex, the Paleoproterozoic Dakendaban Group, and the Mesoproterozoic Wandonggou Group. These are in tectonic contact with each other and are all unconformably covered by the Neoproterozoic Quanji Group as well as some Paleozoic to Mesozoic sedimentary strata (Lu et al., 2006; Chen et al., 2009, 2012; Wang et al., 2009). The Delingha Complex comprises 2.39–2.24 Ga granitic gneisses with variable-scale enclaves of amphibolite and felsic gneiss as well as mafic granulite (Chen et al., 2012). The Wandonggou Group consists of greenschist-facies volcanic–sedimentary rocks and yields an Rb–Sr isochron age of 1022 ± 64 Ma (Yu et al., 1994). The Dakendaban group comprises upper amphibolite- to granulite-facies volcanic–sedimentary and supracrustal rocks and is divided into the lower Dakendaban sub-Group and the upper sub-Group by Chen et al. (2012).

Zircon U–Pb geochronology and regional stratigraphic correlations were used to suggest that the North Wulan gneiss complex represented the basement of the Oulongbuluke microcontinental block (Chen et al., 2009) and was considered to be a part of the Dakendaban group (Lu et al., 2006; Chen et al., 2009, 2012; Wang et al., 2009). However, the North Wulan gneiss complex has been recently regarded as an independent terrane because it has a younger

metamorphic basement than the southwestern Oulongbuluke microcontinental block, and contains Mesoproterozoic, Neoproterozoic and early Paleozoic rocks (Li et al., 2015a, b; Wang et al., 2016; Yu et al., 2017c).

2.2. North Wulan gneiss complex

The North Wulan gneiss complex consists of granitic gneiss, pelitic gneiss, amphibole-biotite gneiss, quartzite, and marble with minor amphibolite and mafic granulite lenses in the granitic and pelitic gneiss (Fig. 1c). The North Wulan gneiss complex is strongly deformed and contains upper amphibolite- to granulite-facies assemblages along with associated migmatites (Guo et al., 2009; Li et al., 2015a, b; Da et al., 2017). Peak metamorphic conditions of a sillimanite-garnet-biotite-plagioclase gneiss in the North Wulan gneiss complex were estimated at 680–700°C at 3.5–4.2 kbar based on Grt–Bt–Pl–Qtz thermobarometry (Li et al., 2015a). Zircon U–Pb geochronology brackets the timing of metamorphism between 483 and 450 Ma (Li et al., 2015a). Multiple episodes of magmatism occurred in the North Wulan gneiss complex, including in the Mesoproterozoic, early Neoproterozoic, early Paleozoic and Mesozoic (Sun et al., 2015; Kang et al., 2015; Wang et al., 2016; Cheng et al., 2015). Pre-Mesozoic magmatic rocks are deformed and metamorphosed to variable degrees (Wang et al., 2016). Gray gneisses with low-Al tonalite–trondhjemite–granodiorite compositions yielded U–Pb zircon crystallization ages of 1519 ± 5 Ma and 1497 ± 8 Ma, which were proposed to record the initial fragmentation of the supercontinent Columbia (Wang et al., 2016). Early Paleozoic magmatic rocks include gabbro, gabbro-diorite and granite (Kang et al., 2015; Sun et al., 2015), whereas the Mesozoic intrusions are mainly composed of granodiorite, quartz diorite, granite

and gabbro (Guo et al., 2009; Cheng et al., 2015). Therefore, the North Wulan gneiss complex contains multiple generations of magmatic activity. However, the timing and nature of partial melting in the North Wulan gneiss complex as well as the temporal relationship of anatexis to magmatic activity are still unclear.

3. Sample descriptions and petrography

Gabbroic–dioritic migmatite is ubiquitous in the North Wulan gneiss complex and this unit is separated from metasandstone and marble by thrust faults (Fig. 2a). A pervasive foliation (S_1) in the migmatites is defined by the parallel alignment of biotite grains and strikes ~135° dipping towards the SW at ~65°. The gabbroic–dioritic migmatite has three components: amphibole-biotite gneiss, leucosome and melanosome (Fig. 2b). Mineral abbreviations used in the text and figures are from Whitney and Evans (2010).

Amphibole-biotite gneiss is composed of amphibole, plagioclase, biotite and quartz, with accessory ilmenite, zircon, apatite, and titanite (Fig. 3a). Amphibole typically contains corroded and/or rounded inclusions of plagioclase, biotite, quartz and rare clinopyroxene (Fig. 3b). Biotite has irregular margins and locally forms clusters in the matrix (Fig. 3a). Locally, titanite reaches modes of up to 5 vol% (Fig. 3a). Coarse-grained plagioclase contains abundant inclusions of fine-grained and rounded plagioclase, quartz, and biotite, locally with inclusions of amphibole and clinopyroxene (Fig. 3c). Cores of coarse-grained plagioclase contain irregular polymineral inclusion of biotite + quartz + plagioclase, which may represent former anatectic melt trapped by plagioclase during growth (Fig. 3d). Cuspate and elongate feldspar and quartz grains are distributed along grain boundaries between biotite and amphibole (Fig.

3e), which are interpreted to represent pseudomorphs of former melt (e.g. Sawyer, 2010; Yu et al., 2015). Rare anhedral clinopyroxene is surrounded by amphibole giving rise to a mottled texture (Fig. 3f). This texture occurs only in the most mafic varieties of gabbroic–dioritic protolith, which suggests that the clinopyroxene may be inherited from the igneous protolith.

Melanosomes are volumetrically minor and occur locally along leucosome margins or within leucosomes (Fig. 2c). The mineral assemblage of the melanosomes includes amphibole, biotite, plagioclase, and minor quartz, with accessory magnetite, ilmenite, zircon, apatite, and titanite. Generally, melanosomes contain a mineral assemblage that is similar to the amphibole-biotite gneiss, but with higher proportions of amphibole, biotite and titanite.

Leucosomes form 1–50 cm thick layers that are a few meters in length (Fig. 2d). They are medium- to coarse-grained and locally folded (Fig. 2e). Most leucosomes are concordant with the dominant foliation and some are discordant (Fig. 2d, f). The proportion of leucosome in outcrop generally ranges from 5 to 40 vol. % with up to 40–50 vol. % locally. Leucosomes contain enclaves of melanosome (Fig. 2c). Leucosome forms an anastomosing network (Fig. 2g). Small and irregular leucosome patches consisting of Pl + Kfs + Qtz are also observed in outcrop. These patches are 10–20 cm across, have diffuse boundaries with amphibole-biotite gneiss, locally contain coarse-grained amphibole (Fig. 2h), and are interpreted to represent *in situ* leucosome. Leucosomes contain variable proportions of plagioclase, K-feldspar, quartz and minor biotite and/or amphibole, with accessory zircon and apatite. Most quartz grains are located in interstices between frameworks of plagioclase and K-feldspar. Biotite grains contain irregular grain boundaries and appear resorbed (Fig. 3g). Some leucosomes contain blocky plagioclase with interstitial K-feldspar and quartz (Fig. 3h).

4. Analytical methods

Detailed analytical methods are found in the Electronic Appendix 1. Whole-rock major and trace element analyses were performed at the State Key Laboratory of Continental Dynamics, Northwest University, Xi'an, China. Zircon U–Pb geochronology of two amphibole-biotite gneiss samples and eight leucosome samples was conducted by LA-ICP-MS at the School of Resources and Environmental Engineering, Hefei University of Technology or by SHRIMP at the Beijing SHRIMP Center, Chinese Academy of Geological Sciences. Trace element analyses of zircon were measured by LA-ICP-MS at the School of Resources and Environmental Engineering, Hefei University of Technology and Hf isotopes in zircon were measured by LA-MC-ICP-MS at the Institute of Geology and Geophysics, Chinese Academy of Sciences in Beijing. Electronic Appendix 2 contains whole-rock major and trace element data. The SHRIMP and LA-ICP-MS zircon U–Pb data are given in Electronic Appendix 3. The results of zircon trace element analysis are presented in Electronic Appendix 4. The Lu–Hf isotopic data are provided in Electronic Appendix 5.

5. Results

5.1. Whole rock geochemistry

5.1.1. Amphibole-biotite gneiss

Amphibole-biotite gneiss samples have concentrations of SiO_2 ranging from 54.4 to 55.2 wt% (Fig. 4), and are metaluminous with aluminum saturation indices (ASI = molar Al_2O_3 /[CaO + Na_2O + K_2O]) of 0.75–0.83 (Electronic Appendix 2). Their chondrite-normalized rare

earth elements (REE) patterns are characterized by a slight enrichment of the light rare earth elements (LREE) ($(La/Yb)_N$ = 5.01–7.76, $(Dy/Yb)_N$ = 1.34–1.35) with minor negative Eu anomalies (Fig. 5a). They show slight depletions in high field-strength elements (HFSE) (e.g. Nb, Ta, Zr and Hf) relative to primitive mantle (Fig. 5b). The amphibole-biotite gneisses have similar major and trace element compositions to the melanosomes, but contain slightly higher concentrations of SiO_2, and slightly lower concentrations of $Fe_2O_3^T$ and P_2O_5 (Figs. 4, 5).

5.1.2. Melanosome

Melanosomes are moderately metaluminous with ASI values between 0.66 and 0.78 and have concentrations of SiO_2 ranging from 51.0 to 52.6 wt% (Fig. 4; Electronic Appendix 2). Compared to the leucosomes, melanosomes have higher concentrations of TiO_2, $Fe_2O_3^T$, MgO, CaO, P_2O_5, and relatively low concentrations of K_2O, and nearly equivalent concentrations of Na_2O (Fig. 4). Melanosomes have $(La/Yb)_N$ values of 7.93–11.1, $(Dy/Yb)_N$ values of 1.40–1.62, and minor negative Eu anomalies (Fig. 5a). Primitive-mantle normalized trace element patterns show positive Nb and Ta anomalies and moderate to negative Sr and P anomalies (Fig. 5b). Compared with leucosomes, the melanosomes are relatively enriched in CaO + Na_2O but depleted in K_2O.

5.1.3. Leucosome

Leucosomes have concentrations of SiO_2 ranging from 63.6 to 75.2 wt%, which are higher than concentrations in the amphibole-biotite gneisses and melanosomes (Fig. 4). Leucosomes also have relatively high ASI values of 0.92–1.06 with an average value of 1.01 (Electronic Appendix 2). Compared with amphibole-biotite gneisses, leucosomes have higher

concentrations of K_2O, similar Na_2O values, and lower concentrations of Al_2O_3, CaO, P_2O_5, TiO_2, $Fe_2O_3^T$ and MgO (Fig. 4). Variation diagrams show decreasing concentrations of TiO_2, P_2O_5, (FeO^T + MgO + TiO_2) and (CaO + Na_2O) with increasing SiO_2 (Fig. 6a–c, e). Both K_2O and Na_2O show no systematic changes with increasing SiO_2. K_2O covaries with (CaO + Na_2O) (Fig. 6d), which is similar to the trend on the (CaO + Na_2O) vs. SiO_2 diagram (Fig. 6e).

Concentrations of Sr, Rb, and Ba are negatively correlated with SiO_2 (Fig. 6f–h), whereas La, Zr, U and Th show no clear trends. Vanadium is positively correlated with increasing TiO_2 (Fig. 7a). P_2O_5 is weakly correlated with increasing LREE, and Th covaries with concentrations of the LREE (Fig. 7b, c). There is no distinguishable correlation between Zr and the heavy rare earth elements (HREE), but Y is positively correlated with increasing HREE (Fig. 7d). Positive correlations between Zr and Hf as well as between Zr and U are apparent in Fig. 7e, f.

Leucosomes display lower concentrations of REE relative to amphibole-biotite gneisses and melanosomes, and are divided into three groups based on their distinct REE patterns (Fig. 5c). Group 1 has the lowest concentrations of REE with notable positive Eu anomalies and flat HREE patterns ($(Dy/Yb)_N$ = 0.80–1.82). They have prominent positive Sr anomalies on the primitive mantle-normalized diagram (Fig. 5d). This group has moderate Sr concentrations of 232–362 ppm and extremely low concentrations of Y (2.06–3.60 ppm), which results in the highest Sr/Y ratios of any group. Group 2 has the highest LREE concentrations with slight positive or negative Eu anomalies. Samples from this group exhibit highly fractionated REE patterns with $(La/Yb)_N$ = 31–174 and $(Dy/Yb)_N$ = 1.36–3.58 and have relatively high concentrations of Sr (171–434 ppm) and moderate concentrations of Y (4.11–9.52 ppm), which results in moderate Sr/Y ratios. Group 3 has the highest concentrations of HREE with the

flattest REE patterns ($(La/Yb)_N$ = 6.56–7.69) and negligible Eu anomalies. This group has the lowest Sr/Y ratios resulting from moderate concentrations of Sr (345–415 ppm) and high concentrations of Y (16.4–21.9 ppm).

5.2. Zircon U–Pb geochronology and trace elements

5.2.1. SHRIMP U–Pb

Representative cathodoluminescence (CL) images of zircons analyzed by SHRIMP are shown in Fig. 8. The results of SHRIMP zircon U–Pb geochronology are reported in Electronic Appendix 3 and are plotted on Concordia diagrams in Fig. 9.

Zircons from leucosome sample 11RLD7 (37°05′29″N, 98°51′48″E) form short prismatic and stubby grains 150–350 μm in length with oscillatory zoning in CL (Fig. 8a). Fourteen analyses yield a range of dates from 479 to 448 Ma (with three dates of 511, 507 and 494 Ma), with a dominant group of 11 concordant dates that have relatively low Th/U ratios (0.05–0.55) and yield a weighted mean age of 465.2 ± 6.5 Ma (MSWD = 1.9) (Fig. 9a). This age is interpreted to date crystallization of the leucosome. Three older dates of 511, 507 and 494 Ma are interpreted to be inherited from the amphibole-biotite gneiss.

Zircons from leucosome sample 11RLD12 (37°05′28″N, 98°51′49″E) are dominantly acicular to prismatic, subhedral to euhedral grains, and are subdivided into two types based on internal structure (Fig. 8b). Type I zircons show no core–rim structures, have pronounced oscillatory zoning, and yield a range of dates from 470 to 437 Ma with Th/U ratios of 0.18–0.52. Type II zircons have small rounded cores with uniform dark-CL rim overgrowths without oscillatory zoning. The inherited cores have relatively high Th/U ratios (0.2–0.7) and yield

various U–Pb ages of 1672–951 Ma. The dark-CL rims of zircon have relatively low Th/U ratios (0.04–0.21) and yield a range of dates from 480 to 466 Ma. Nine analyzed spots from Type 1 zircon and the dark-CL rims in Type 2 zircon yield a weighted mean $^{206}Pb/^{238}U$ age of 464.2 ± 8.4 Ma (MSWD = 2.5) (Fig. 9b), which is interpreted as the crystallization age of the leucosome.

Oscillatory-zoned zircons from leucosome sample 11RLD19 (37°05′29″N, 98°51′20″E) are prismatic to stubby and subhedral to euhedral (Fig. 8c). Twelve analyzed zircon grains show relatively high Th/U ratios (0.05–0.57) and have $^{206}Pb/^{238}U$ ages ranging from 474 to 439 Ma. These 12 spots yield a weighted mean $^{206}Pb/^{238}U$ age of 454.6 ± 5.6 Ma (MSWD = 1.6) (Fig. 9c), which is interpreted to date crystallization of the leucosome.

Zircons from leucosome sample 11RLD20 (37°05′28″N, 98°51′21″E) are euhedral and prismatic with oscillatory zoning in CL (Fig. 8d). Ten of 12 spot analyses range from 446 to 441 Ma and yield a weighted mean age of 453.5 ± 5.7 Ma (MSWD = 1.2), with two $^{206}Pb/^{238}U$ dates of 505 and 424 Ma (Fig. 9d). The weighted mean age is interpreted to represent the time of leucosome crystallization. The 505 Ma date is interpreted to represent inheritance from the amphibole-biotite gneiss, whereas the 424 Ma date is interpreted to reflect radiogenic Pb loss and is not geologically meaningful.

5.2.2. LA-ICP-MS

Two amphibole-biotite gneiss (12ELH4 and 12ELH15) and four leucosome samples (12ELH3, 12ELH5, 12ELH12 and 12ELH14) were selected for zircon U–Pb geochronology and trace elements analysis by LA-ICP-MS. Representative CL images are shown in Fig. 10.

Zircon U–Pb data are reported in Electronic Appendix 3, and plotted on Concordia diagrams in Fig. 11. Zircon trace element data is reported in Electronic Appendix 4 and chondrite-normalized REE concentrations are plotted in Fig. 12.

Zircons in amphibole-biotite gneiss sample 12ELH4 (37°05′28″N, 98°51′53″E) are stubby to elongate, prismatic and minor oval grains that are 150–400 μm in length (Fig. 10a). Most zircons exhibit core–rim structures with CL-dark cores surrounded by bright luminescent rims in CL. The CL-dark cores are characterized by oscillatory zoning (Fig. 10a), and high Th/U ratios (generally >0.5), which are typical features of magmatic zircon (e.g. Corfu et al. 2003). Most CL-bright rims are too thin to be analyzed by laser ablation. Thirty-four laser ablation analyses were obtained from 33 grains. Thirty-three analyses conducted on cores yielded $^{206}Pb/^{238}U$ dates ranging from 521 to 489 Ma with a weighted mean age of 503.5 ± 4.6 Ma (MSWD = 0.5) (Fig. 11a), which is interpreted as the crystallization age of the protolith of the amphibole-biotite gneiss. One date from a zircon rim yields a concordant $^{206}Pb/^{238}U$ age of 453 Ma, which is interpreted as the timing of metamorphism. All analyzed spots have similar negative Eu anomalies, positive Ce anomalies and enriched HREE patterns (Fig. 12a). Rims have lower REE concentrations than the cores.

Zircons from amphibole-biotite gneiss sample 12ELH15 (37°05′51″N, 98°52′05″E) are predominantly oval and prismatic and are 80–200 μm in length. Most grains contain blurred oscillatory-zoned and partially resorbed cores in CL with bright rims that truncate the CL-dark cores to varying degrees (Fig. 10b). Twenty-nine spots analyzed on CL-dark cores have relatively high Th/U ratios (generally >0.5) and high REE contents (Fig. 12b), and yield $^{206}Pb/^{238}U$ ages varying from 518 to 484 Ma with a weighted mean of 506.2 ± 4.9 Ma (MSWD

= 0.29) (Fig. 11b), reflecting the time of crystallization of the protolith. The two younger dates of 452 and 450 Ma were obtained from CL-bright rims with relatively low Th/U ratios (0.16 and 0.35) and low REE contents (Fig. 12b). These dates are interpreted to record the timing of metamorphism and anatexis. Both cores and rims have negative Eu and positive Ce anomalies, and enriched HREE patterns (Fig. 12b)

Zircons from leucosome sample 12ELH3 (37°05′29″N, 98°51′52″E) are euhedral, isometric or elongate grains with lengths of 200–400 μm. Most zircons exhibit strong oscillatory zoning in CL (Fig. 10c). Twenty-eight spots analyzed on these zircons have variable Th/U ratios of 0.06–0.45, and give $^{206}Pb/^{238}U$ ages ranging from 475 to 453 Ma, with a weighted mean of 465.3 ± 4.5 Ma (MSWD = 0.25) (Fig. 11c), which is interpreted to date the crystallization of the leucosome. In addition, an older $^{206}Pb/^{238}U$ age of 508 Ma was obtained from an oscillatory-zoned zircon (Fig. 10c) with a Th/U ratio of 0.27, which is interpreted to be inherited from protolith. All analyzed spots show negative Eu and positive Ce anomalies and have similar HREE patterns, but have variable concentrations of LREE (Fig. 12c).

Zircons from leucosome sample 12ELH5 (37°05′29″N, 98°51′52″E) are subhedral to euhedral, and are prismatic in shape with lengths of 100–350 μm. CL images reveal that most of these zircons have relatively homogeneous luminescence from core to rim with pronounced oscillatory zoning (Fig. 10d). A few zircons have bright-luminescent irregular-shape (inherited) cores surrounded by gray-luminescent (magmatic) rims with diffuse zoning. Thirty analyses on CL-homogeneous zircons and the magmatic rims have relatively low REE contents and Th/U ratios (generally <0.4), and yield $^{206}Pb/^{238}U$ ages varying from 475 to 441 Ma, with a weighted mean of 454.9 ± 4.3 Ma (MSWD = 0.55) (Fig. 11d). Five analyses of the cores display

relatively high REE contents and Th/U ratios (generally >0.5), and have $^{206}Pb/^{238}U$ ages varying between 522 and 496 Ma with a weighted mean of 503 ± 11 Ma (MSWD = 0.7). All analyses yield positive Ce and negative Eu anomalies, variable concentrations of LREE and have enriched HREE patterns. Concentrations of REE in the inherited cores are relatively higher than those in the newly formed zircons and zircon rims (Fig. 12d).

Zircons in leucosome 12ELH12 (37°05′50″N, 98°52′06″E) are euhedral, prismatic and oscillatory zoned in CL with grain sizes ranging from 200 to 400 μm (Fig. 10e). Except for two spots with older ages of 500 and 488 Ma, twenty-nine analyses yield $^{206}Pb/^{238}U$ ages varying between 479 and 448 Ma, have relatively low Th/U ratios (0.05–0.51), and give a weighted mean age of 458.6 ± 4.4 Ma (MSWD = 0.56) (Fig. 11e), which is interpreted to represent the crystallization age of leucosome. Two older dates of 500 Ma and 488 Ma likely reflect inheritance from the protolith. All zircons display negative Eu and positive Ce anomalies with enriched concentrations of HREE, but have different LREE patterns (Fig. 12e).

Zircons from leucosome sample 12ELH14 (37°05′51″N, 98°52′05″E) are euhedral and elongate with lengths of 100–300 μm. CL images reveal that most zircons have clear oscillatory zoning and some contain core–rim structures (Fig. 10f). All of the twenty-nine U–Pb analyses exhibit relatively high but variable Th/U ratios (0.18–0.55). Except for two analyzed spots from inherited cores, which show relatively old $^{206}Pb/^{238}U$ ages of 528 and 518 Ma, the remaining 27 analyses have $^{206}Pb/^{238}U$ ages varying from 474 to 440 Ma with a weighted mean age of 460.6 ± 4.5 Ma (MSWD = 0.63) (Fig. 11f). All of these analyses show enriched concentrations of the HREE and variable concentrations of the LREE (Fig. 12f)

5.3. Zircon Lu–Hf isotopes

The results of Lu–Hf isotope analysis on zircon from three amphibole-biotite gneiss (amphibole-biotite gneiss samples 11RLD10 and 11RLD18 are dated by Li et al. (2015b)) and four leucosome samples are presented in Electronic Appendix 5 and are shown in Fig. 13. The locations of Lu–Hf isotope analyses are shown in Figs 8 and 10. Forty-nine analyses on magmatic cores of zircon grains from three amphibole-biotite gneiss samples have initial $^{176}Hf/^{177}Hf$ ratios of 0.282360–0.282559 and $\varepsilon Hf_{(t)}$ values of -3.5 to +3.6 calculated at the individual mean ages of zircon cores. Their corresponding single-stage Hf model ages (T_{DM1}) and two-stage Hf model ages (T_{DM2}) are 1.3–1.0 and 1.7–1.2 Ga, respectively. Nine analyses on metamorphic rims from three amphibole-biotite gneiss samples have initial $^{176}Hf/^{177}Hf$ ratios that vary from 0.282400 to 0.282480 and $\varepsilon Hf_{(t)}$ values that range from -3.3 to -0.4. Thirty-two analyses on the newly formed zircons and zircon rims from three leucosome samples (11RLD7, 11RLD19 and 11RLD20) yield initial $^{176}Hf/^{177}Hf$ ratios of 0.282401–0.282496 and $\varepsilon Hf_{(t)}$ values of -2.9 to +0.2 calculated at the individual mean ages of magmatic zircon rims, corresponding to T_{DM1} model ages of 1.2–1.0 Ga and T_{DM2} model ages of 1.6–1.4 Ga. Four analyses of inherited cores yield initial $^{176}Hf/^{177}Hf$ ratios of 0.282416–0.282516, and $\varepsilon Hf(t)$ values of -1.6 to +2.1. These cores yield T_{DM1} model ages of 1.2–1.0 Ga and T_{DM2} model ages of 1.6–1.3 Ga.

Lu–Hf isotope analyses were also conducted on zircons with inherited Precambrian cores from sample 11RLD12. Nine spots on the newly formed zircons and zircon rims give initial $^{176}Hf/^{177}Hf$ ratios that vary from 0.282417 to 0.282466 and $\varepsilon Hf(t)$ values that range from -2.3 to -0.6, which corresponds to T_{DM1} ages of 1.2–1.1 Ga and T_{DM2} ages of 1.6–1.5 Ga. Three

analyses on inherited Precambrian cores have $^{176}Hf/^{177}Hf$ ratios and $\varepsilon Hf_{(t)}$ values ranging from 0.281857 to 0.282272 and -7.6 to +5.6, respectively. These three analyses yield T_{DM1} model ages of 1.9–1.4 Ga and T_{DM2} model ages of 2.3–1.5 Ga.

6. Discussion

6.1. Protolith of the migmatites

Zircon is an extremely stable mineral that has a high closure temperature for Pb diffusion (Cherniak and Watson, 2003). Thus, zircon U–Pb geochronology of amphibole-biotite gneiss and leucosome combined with zircon morphology represent a reliable means to determine the age of the protolith and the timing of partial melting. Zircons from two amphibole-biotite gneiss samples in this study and from two amphibole-biotite gneiss samples (11RLD10 and 11RLD18) from Li et al. (2015b) show core–rim structures (Figs. 8, 10). CL-bright rims truncate CL-dark cores. The CL-dark cores are characterized by oscillatory zoning (Figs. 8, 10) and relatively high Th/U ratios, which are typical of magmatic zircon. These zircons also have enriched HREE and negative Eu anomalies (Fig. 12a, b), which also supports a magmatic origin for the CL-dark cores. These cores yield U–Pb ages of 504 ± 5 (Li et al. 2015b), 494 ± 5 (Li et al. 2015b), 504 ± 5 and 506 ± 5 Ma (Fig. 11a, b), which are interpreted to represent the crystallization age of the magmatic protolith. These provide unambiguous evidence that not all of migmatitic gneisses in the North Wulan gneiss complex have Precambrian protoliths. The age of the protolith of the migmatitic amphibole-biotite gneiss in this study is almost the same age as early Paleozoic island arc volcanic rocks in the South Qilian–North Qaidam orogenic belt (*ca.* 514 Ma; e.g. Shi et al., 2006). Therefore, the protoliths of the migmatites may also

represent remnants of Cambrian arc magmatism in an active continental margin.

Zircon U–Pb ages of 528–488 Ma from most inherited zircon cores in leucosome samples also indicate that the protolith of the migmatites formed in the early Paleozoic. However, the age of inherited zircon cores from leucosome sample 11RLD12 is different from the other leucosome samples (Fig. 9b). Zircon from sample 11RLD12 yield four U–Pb ages ranging from 1672 to 951 Ma with relatively high Th/U ratios (0.2–0.7). There is no similar-aged zircon found in the amphibole-biotite gneiss. Therefore, we speculate that these inherited zircons may be sourced from the underlying metasedimentary country rock (e.g. metasandstone) either during partial melting of this unit or the scavenging of detrital zircons during melt migration through it. Considering that this is the only sample (out of 8 dated leucosome samples) that contains inherited Precambrian zircon, we exclude this sample from the discussion of the age of the protolith and the petrogenesis of the migmatites. However, we do not rule out the possibility of a minor contribution of partial melting of the underlying metasedimentary rocks to the leucosomes found in the North Wulan gneiss complex.

Hafnium isotopic analyses of zircon cores from three amphibole-biotite gneiss samples yield εHf(t) values of -3.5 to +3.6 and T_{DM1} ages of 1.3–1.0 Ga, corresponding to two-stage Hf model ages (T_{DM2}) of about ~1.7–1.2 Ga with most between 1.6 and 1.4 Ga (Electronic Appendix 5). This suggests that the protolith was derived from reworking of Meso-Neoproterozoic crust. Leucosomes in amphibole-biotite gneiss are interpreted to have formed in a closed isotopic system during partial melting (see discussion below), and thus their Hf isotopic compositions can be used to decipher their sources (Schmidberger et al., 2005; Zheng et al., 2006). Zircons from three leucosome samples (11RLD7, 11RLD19 and 11RLD20) yield

mean T_{DM2} ages of ~1.5–1.4 Ga (Electronic Appendix 5), which also suggests that their magmatic protoliths were formed by reworking of Mesoproterozoic crust. Low-Al trondhjemitic gneisses exposed in the North Wulan gneiss complex yield crystallization ages of ~1.5 Ga, which are interpreted to record the initial fragmentation of the Columbia supercontinent (Wang et al., 2016). Zircon Hf T_{DM2} ages of the amphibole-biotite gneiss in this study together with the age of low-Al trondhjemitic gneisses is consistent with the presence of a Mesoproterozoic basement beneath the North Wulan gneiss complex.

6.2. Timing of partial melting

Anatexis can be related to magmatic underplating, continental extension, and thinning of the lithosphere, and thus the timing of anatexis is crucial for understanding the timing of orogenesis in the South Qilian–North Qaidam orogenic belt. Zircon U–Pb geochronology of leucosomes constrains the timing of partial melting in the North Wulan gneiss complex. Zircons from four leucosome samples exhibit relatively steep chondrite-normalized REE patterns and negative Eu anomalies (Fig. 12c–f), implying that they grew in the presence of plagioclase and were not in equilibrium with garnet (Rubatto et al., 2009). Relatively high but variable Th/U ratios in zircon may reflect the dissolution of Th-bearing mineral phases (e.g. monazite or allanite) or may be inherited from their protoliths (e.g. Bröcker et al., 2010; Yakymchuk et al., 2018). Zircons from these leucosome samples show oscillatory zoning and contain inherited zircon cores that yield the same ages as the protolith. Therefore, the ages of leucosome samples constrain the timing of melt crystallization and zircon growth.

Seven leucosome samples yield zircon U–Pb ages ranging from 465 to 454 Ma (Figs. 9a,

c, d, 11c-f), which is interpreted to represent the timing and minimum duration of melt crystallization (e.g. Kelsey et al., 2008; Yakymchuk and Brown, 2014), and the approximate timing of metamorphism and anatexis. Metamorphic rims of zircon from four amphibole-biotite gneiss samples yield ages of 466–450 Ma (Fig. 11a, b; Li et al. 2015b), which are roughly consistent with the crystallization age of the leucosome. Together, these ages are older than the timing of high-pressure granulite-facies partial melting (438–428 Ma) recorded by zircon in leucosome and tonalite in the Dulan area (Yu et al., 2012, 2014), but these ages overlap with the timing of high-temperature/low-pressure metamorphism previously reported in the North Wulan gneiss complex (483–450 Ma; Li et al., 2015a). The timing of metamorphism and anatexis in this study is also contemporaneous with the crystallization of *ca.* 470–444 Ma arc-related granitoids in the South Qilian–North Qaidam orogenic belt formed by northward subduction of South Qilian oceanic crust (Wu et al., 2009, 2014). Taking all these ages into consideration, we suggest that the North Wulan gneiss complex was subjected to metamorphism and anatexis at *ca.* 465 to 450 Ma.

6.3. Petrogenesis of the migmatites

The Lu–Hf system in zircon is highly robust during most geological processes including anatexis (Gerdes and Zeh, 2009) and melts can inherit Hf isotope ratios from their source rocks (Corfu and Noble, 1992). Therefore, Hf isotope compositions of zircon in migmatites can be used to trace the origin of the protolith and evaluate if partial melting occurred in a closed or open isotopic system (e.g. Flowerdew et al., 2006; Wu et al., 2007).

For amphibole-biotite gneiss and leucosome samples from the North Wulan gneiss

complex, the spread of initial $^{176}Hf/^{177}Hf$ ratios and $\varepsilon Hf_{(t)}$ values are less for the metamorphic rims and anatectic rims than the cores (Fig. 13e, f; Electronic Appendix 5). This suggests that zircon from the protolith contains more Hf isotopic heterogeneity than metamorphic zircon and anatectic zircon. Hf isotope compositions of zircon from leucosome samples exhibit relatively small variations in initial $^{176}Hf/^{177}Hf$ ratios from grain to grain (Fig. 13a, b), which suggest that Hf isotopes were homogenized in the anatectic melt (e.g. Flowerdew et al., 2006). Initial $^{176}Hf/^{177}Hf$ ratios and $\varepsilon Hf_{(t)}$ ratios of metamorphic rims of zircons in amphibole-biotite gneiss samples are similar to those of the newly formed zircons and zircon rims in the leucosomes (Fig. 13e, f; Electronic Appendix 5). This suggests that isotopic equilibrium was achieved between the amphibole-biotite gneiss and the leucosome during the growth of anatectic zircon.

Zircons from different leucosome samples display similar Hf isotope ratios except for spot #8 in sample 11RLD20, which has much higher initial $^{176}Hf/^{177}Hf$ and $\varepsilon Hf_{(t)}$ values (Fig. 13a–d; Electronic Appendix 5). However, this exceptional value has a very high associated analytical error (Electronic Appendix 5), which, when considered, puts it within the spread of the other values. The overlapping Hf isotope values of zircons from different leucosomes suggest that they were derived from similar source rocks. Although the Hf isotope compositions are similar between leucosome samples, there are subtle differences indicating local Hf isotope heterogeneity rather than system-scale heterogeneity (e.g. Tang et al., 2014).

There are several possible sources of hafnium that can be incorporated into growing zircon in migmatites. Hafnium can be sourced from: (1) the dissolution of pre-existing zircon (Andersson et al., 2002; Flowerdew et al., 2006), (2) the breakdown of hafnium-rich minerals such as garnet, apatite, amphibole, and titanite in a closed system (Fraser et al., 1997;

Flowerdew et al., 2006), and (3) externally derived melt in an open system (Foster et al., 2001; Zheng et al., 2006). Hf isotope values of externally derived melt can be highly variable because of the large variety of potential sources. However, in a closed system, zircon dissolution is expected to release Hf to the melt during anatexis, and this Hf will be incorporated into growing zircon during melt crystallization. Therefore, in a closed anatectic system, newly crystallized zircons are predicted to have similar Hf isotope ratios to the precursor zircons (e.g. Yakymchuk et al., 2015).

If leucosomes in the North Wulan gneiss complex are derived from partial melting of different sources rather than the amphibole-biotite gneiss, there should be different zircon Hf isotopic compositions among them. However, in amphibole-biotite gneiss samples (11RLD10, 11RLD18 and 12ELH4), zircon metamorphic rims yield initial $^{176}Hf/^{177}Hf$ ratios and $\varepsilon Hf_{(t)}$ values compatible with those of their inherited cores (Fig. 13e, f; Electronic Appendix 5). In leucosome samples 11RLD7 and 11RLD20, the newly formed zircons and zircon rims have indistinguishable initial $^{176}Hf/^{177}Hf$ ratios and $\varepsilon Hf_{(t)}$ values from those of the inherited cores (Fig. 13a–d; Electronic Appendix 5).

If the source of Hf was the breakdown of other Hf-bearing minerals rather than pre-existing zircons, then new magmatic zircons or overgrowth rims would be expected to have more radiogenic $^{176}Hf/^{177}Hf$ values due to the higher Lu/Hf ratios of these other minerals (Flowerdew et al., 2006; Gerdes and Zeh, 2009). Dissolution textures from zircon cores in both amphibole-biotite gneiss and leucosome in the North Wulan gneiss complex (Figs. 8, 10) demonstrate that pre-existing zircons were partially dissolved during partial melting of the protolith (e.g. Williams, 2001; Flowerdew et al., 2006). In addition, the ages of inherited zircon in leucosome

are consistent with the crystallization age of the amphibole-biotite gneiss. Although the inherited zircons could be derived from other sources with the same age as the amphibole-biotite gneiss, the coherent Hf isotope composition between the inherited zircons and overgrowth rims makes this possibility less likely.

Considering the presence of inherited zircons in leucosomes, indistinguishable Hf-isotope signatures between the inherited zircons and overgrowth rims, and apparent dissolution textures in zircon, the Hf budget of the melt from which new zircon crystallized is dominantly derived from the breakdown of pre-existing (igneous) zircon. Therefore, a closed isotopic system likely existed during anatexis.

6.4. Melting reaction

Anatexis can occur through the breakdown of hydrous minerals, such as muscovite, biotite or amphibole (Thompson, 1982); through the influx of an externally derived fluid (Weinberg and Hasalová, 2015); or, through the breakdown of anhydrous minerals at ultrahigh temperature conditions (e.g. Kelsey et al., 2015). Hydrate-breakdown melting is generally considered to represent the principal process that generates granitic melts in the lower to middle crust (Clemens and Vielzeuf, 1987). However, water-fluxed melting is also widely recognized as a crucial process in the evolution of many anatectic terranes (Reichardt and Weinberg, 2012; Wang et al., 2013; Lee and Cho, 2013; Weinberg and Hasalová, 2015). Experimental studies suggest that the presence of an H_2O-bearing fluid can decrease the temperature of the solidus and melting of biotite-bearing rocks in the presence of hydrous fluid at 6 kbar begins at temperatures of about 680 °C (Watkins et al., 2007). In intermediate to basic compositions,

water-fluxed melting and the growth of peritectic amphibole are predicted to take place at temperatures below the transition between amphibolite and granulite facies. Petrographic evidence of this reaction includes coarse-grained amphibole with inclusions of resorbed reactant minerals, including: biotite, plagioclase and quartz (Slagstad et al., 2005; Reichardt and Weinberg, 2012; Wang et al., 2013; Hu et al., 2016).

There are four lines of evidence that support fluid-present melting of the gneisses in the North Wulan gneiss complex. First, there are no anhydrous peritectic minerals (e.g. garnet or orthopyroxene) found in the gneisses, which are essential products of incongruent fluid-absent melting reactions in basic and intermediate rocks (e.g. Clemens, 2006). Second, metamorphic zircons are enriched in the HREE (Fig. 12a, b), which would normally be depleted if garnet was in equilibrium with zircon (e.g. Rubatto, 2002). Third, the amount of interpreted *in situ* leucosome (up to 40 vol.%) is too large to be generated from fluid-absent melting alone at amphibolite facies conditions (e.g. Palin et al., 2016). Finally, amphibole contains rounded inclusions of plagioclase, quartz and biotite in migmatitic gneiss (Fig. 3a, b), and titanite is a common accessory mineral in the migmatitic gneiss (Fig. 3a). This assemblage is compatible with the generalized fluid-present melting reaction: Bt + Pl + Qtz + H_2O-rich fluid = Hbl + Pl + Ttn + melt (e.g. Lappin and Hollister, 1980). Coarse-grained plagioclase in the amphibole-biotite gneiss contains abundant inclusions of rounded plagioclase, quartz, and biotite as well as rare inclusions of amphibole and clinopyroxene (Fig. 3c). Except for amphibole and clinopyroxene, this inclusion assemblage is compatible with the reactants of fluid-present biotite-breakdown melting. Inclusions of amphibole in plagioclase (Fig. 3c) may represent early-formed peritectic amphibole that was later included in crystallized plagioclase. Rare

clinopyroxene inclusions in plagioclase may have been inherited from the most mafic varieties of gabbroic–dioritic protolith. Therefore, water-fluxed biotite-breakdown melting is more likely to account for anatexis in the North Wulan gneiss complex than fluid-absent hydrate-breakdown melting.

An important consideration in fluid-present melting is the source of the fluid. The low porosity of the middle–lower crust results in only very minor volumes of free H_2O at high temperature (Yardley and Valley, 1997; Weinberg and Hasalová, 2015). Therefore, if there is no addition of externally sourced H_2O-rich fluid, water-fluxed melting produces a limited quantity of melt in closed system scenarios. However, the abundance of leucosome in the amphibole-biotite gneiss and the requirement of H_2O as a reactant to generate peritectic amphibole suggest that fluid influx induced partial melting. There are three potential sources for the H_2O-rich fluid that facilitated partial melting in the North Wulan gneiss complex. First, the crystallization of gabbro intrusions (472 Ma; our unpublished data) that are coeval with metamorphism in the North Wulan gneiss complex may have provided a heat source as well as exsolved an H_2O-rich fluid. Mantle-derived basaltic magmas from subduction zones are generally enriched in H_2O (Wallace, 2005). This H_2O can be partly transferred into the host rock and induce water-fluxed melting (Annen and Sparks, 2002). Second, evolved granitic melts could release a large amount of H_2O into the wall rock during emplacement (e.g. Morfin et al., 2014). Therefore, the crystallization of contemporaneous granites (464–451 Ma, Sun et al., 2015; our unpublished data) could be a source of water in the North Wulan gneiss complex. Third, subsolidus dehydration of rocks in the deeper crust (e.g. Sawyer, 2010) may have released H_2O that transferred upwards into the North Wulan gneiss complex and induced

partial melting. Alternative sources of H_2O-rich fluids such as seawater or meteoric water are possible, but large-scale extensional structures that could have transported these fluids from the surface to the deep crust (e.g. Wickham and Oxburgh, 1987) are not present in the North Wulan gneiss complex.

Aqueous fluids released from intrusive magmas or dehydration reactions in the deeper crust were likely transported into the North Wulan gneiss complex at temperatures at or above the water-saturated solidus. This process requires a permeable transport conduit for the fluids. Shear zones are widely thought to have a prominent control on water-fluxed melting of granite and orthogneiss and supply the main pathway for the aqueous fluid migration (Genier et al., 2008). The North Wulan gneiss complex was subjected to intense ductile deformation during partial melting and developed numerous small high-strain zones (Guo et al., 2009; Da et al., 2017). Consequently, it is possible that deformation facilitated the migration of aqueous fluids along these shear zones (e.g. Sawyer, 2010). However, the nature and ultimate source of aqueous fluid, and the relationship between water fluxed melting and ductile shearing are still unclear for migmatites in the North Wulan gneiss complex.

6.5. Leucosome composition and melt modification

Many leucosomes in the North Wulan gneiss complex exhibit diffuse boundaries with the host amphibole-biotite gneiss (Fig. 2h), and highly cuspate, elongate feldspar and quartz occur along grain boundaries between biotite and amphibole in the amphibole-biotite gneiss (Fig. 3e). Furthermore, concentrations of major elements in leucosomes from the North Wulan gneiss complex are similar to those generated during water-fluxed melting of dioritic rocks (Fig. 4)

(e.g. Slagstad et al., 2005; Reichardt and Weinberg, 2012; Wang et al., 2013; Hu et al., 2016). Therefore, leucosome in the North Wulan gneiss complex likely represents *in situ* or in source leucosome. In source leucosome represents melt that migrated away from the place of formation and is evolved in composition, but is still within the source rock (e.g. Sawyer, 2008). One possible exception is sample 11RLD12, which contains inherited Precambrian zircon cores (Figs. 8b, 9b) as well as higher concentrations of K_2O, Sr and Rb and lower concentrations of CaO, Na_2O and Ba than the other leucosomes (Electronic Appendix 2). Thus, this sample is inferred to be derived from a different source and is not included in our discussion of leucosome compositions below.

Leucosomes in migmatites are the product of partial melting but may not represent initial (unmodified) melt compositions (e.g. Sawyer, 1987; Solar and Brown, 2001; Brown et al., 2016; Carvalho et al., 2016). Melt modification is a significant process that occurs during melt migration, ascent, and emplacement, and can significantly change the composition of melt from initial values (Solar and Brown, 2001; Clemens and Stevens, 2012; Morfin et al., 2014). Thus, compositional variations of leucosomes can be used to trace the processes that can modify melt compositions. These processes mainly include fractional crystallization, accessory mineral dissolution, and peritectic mineral entrainment (Bea et al., 1994; Zeng et al., 2005; Clemens and Stevens, 2012; Brown et al., 2016).

An important starting point in evaluating the processes that contribute to melt modification in migmatites is the composition of the initial melt (e.g. Sawyer, 2010; Carvalho et al., 2016). To our knowledge, there are no experimental studies of fluid-present melting of mafic-intermediate rocks that apply to the protolith of this study. Of the three groups of leucosomes

from the North Wulan gneiss complex, Group 3 leucosomes do not show strong positive or negative Eu anomalies (unlike Group 1) and do not have highly fractionated LREE patterns, unlike Groups 1 and 2 (Fig. 5c). Furthermore, Group 3 leucosomes do not show blocky feldspar frameworks in thin section. Therefore, we use Group 3 leucosomes as the closest approximation to an initial melt composition.

Accumulation of early-formed feldspars and extraction of the residual melt have a strong control on the compositional evolution of anatectic melts (Sawyer, 1987; Morfin et al., 2014; Brown et al., 2016). Covariation of CaO + Na_2O and K_2O in the leucosomes (Fig. 6d) indicate that they have sodic plagioclase, K-feldspar and quartz on the liquidus (e.g. Morfin et al., 2014). A coherent covariation trend is compatible with fractional crystallization of feldspar. However, the trend shown by leucosomes from the North Wulan gneiss complex is steeper than that defined by the crystallization of plagioclase alone (Fig. 6d), which suggests that another mineral containing less K_2O and minimal CaO and Na_2O is involved (e.g. Morfin et al., 2014). Biotite commonly has irregular and corroded margins and occurs in leucosomes in variable proportions (Fig. 3g), which suggests that the entrainment of residual biotite may be an important control on this trend.

Fractional crystallization also has specific effects on the concentrations of trace elements in leucosome. Europium and the LILE are mainly partitioned into feldspars, but the other REE are generally incompatible with feldspar (Bea et al., 1994). The variation of leucosome REE patterns with positive (Group 1) and negative (Group 2) Eu anomalies (Fig. 5c) may reflect the process of fractional crystallization of feldspar (e.g. Bea et al., 1994). Concentrations of the LILE are negatively correlated with increasing SiO_2 (Fig. 6f–h), which also suggests that the

compositions of leucosomes are controlled by the fractional crystallization of feldspar.

Accessory minerals are the dominant repository for many trace elements (e.g. U, Th, Zr, V, Ti, REE) in silicic rocks and play a crucial role in controlling the distribution of these elements between melt and residue during anatexis and melt crystallization (e.g. Watt and Harley, 1993; Zeng et al., 2005; Yakymchuk and Brown, 2014; Yakymchuk et al., 2017). Covariation between Zr and Hf as well as U and Zr (Fig. 7e, f) suggests that zircon is the main control on the compositions of these elements in leucosomes, especially for Group 1 and Group 2 leucosomes. This is also supported by zircon morphology (Figs. 8, 10); zircons have inherited cores characterized by irregular and corroded margins consistent with dissolution into melt. The LREE are negatively correlated with P_2O_5 (Fig. 7b), which suggests that apatite was an important control on these elements in Groups 1 and 2. However, there is also a covariation between LREE and Th (Fig. 7c), which indicates that monazite may have also contributed.

Titanite is a major sink for some of the HFSE (e.g. Ti, Nb and Ta) and can strongly partition these elements during growth (Storkey, 2005). Covariation between TiO_2 and SiO_2 (Fig. 6a) can be explained by the entrainment of peritectic or residual titanite. The depletion of Nb, Ta and Ti on a primitive-mantle normalized diagram (Fig. 5d) further demonstrates the control of titanite on leucosome compositions. Although rutile could be the dominant control of Nb, Ta and Ti (Linnen and Keppler, 1997), no rutile was observed in amphibole-biotite gneiss. Additionally, a similar covariation between V and TiO_2 (Fig. 7a) suggests that ilmenite was also involved in this process. Both titanite and ilmenite are observed in melanosome, which suggests that titanite and ilmenite jointly influenced the concentrations of TiO_2 in leucosomes.

The entrainment of peritectic minerals is a major control on the composition of monzogranitic to dioritic magmas (Clemens and Stevens, 2012). The melanosome of migmatites is considered a residual mixture of unmelted material and retained peritectic minerals after the extraction of anatectic melt (Sawyer, 2008). The presence of coarse-grained amphibole in the melanosome of migmatites from the North Wulan gneiss complex suggests that some peritectic amphibole was retained in the source. Covariation between (FeO^T + MgO + TiO_2) and SiO_2 in leucosomes (Fig. 6c) may be explained by the segregation of ferromagnesian minerals from anatectic melt (e.g. Morfin et al., 2014). Candidates for these minerals include biotite and amphibole, which are observed in leucosomes (Figs. 2h, 3g). In addition, covariation between HREE and Y (Fig. 7d) may reflect variable entrainment of amphibole (e.g. Reichardt and Weinberg, 2012) in the absence of garnet. Overall, fractional crystallization of feldspar, the entrainment of residual biotite and peritectic amphibole together with the behavior of accessory minerals such as apatite, titanite and zircon led to the distribution of major and trace elements in leucosomes from the North Wulan gneiss complex.

Group 3 leucosomes are interpreted to represent the closest approximation to the initial melt composition. Amphibole grains and amphibole-biotite schlieren (melanosome) are observed in small irregular leucosome patches and at the edge of or in the central part of larger leucosomes in the North Wulan gneiss complex (Fig. 2c, h). This suggests that the entrainment of peritectic amphibole could have led to elevated concentrations of HREE in leucosome (e.g. Reichardt and Weinberg, 2012; Hu et al., 2016). The entrainment of peritectic amphibole is also expected to increase the concentrations of Y, which resulted in relatively low Sr/Y ratios in Group 3 leucosomes.

Group 1 leucosomes are interpreted to represent early-formed feldspar cumulates. They are plagioclase rich and contain cumulate frameworks composed of subhedral to euhedral plagioclase and interstitial quartz grains (Fig. 3h). The high Sr/Y ratios and positive Eu anomalies (Fig. 5c) also reflect the high proportion of plagioclase in Group 1 leucosomes, which is consistent with a cumulate origin.

Group 2 leucosomes represent relatively evolved compositions and may record minor entrainment of peritectic amphibole. Partial melting leaving amphibole in the residue can generate HREE-depleted chondrite-normalized REE patterns (Fig. 5c). This is proposed to account for the highly fractionated REE patterns of Group 2 leucosomes. The high-Sr/Y ratios of Group 2 leucosomes are interpreted to represent plagioclase consumption during water-fluxed melting (e.g. Patiño Douce and Harris, 1998). The slightly positive or negative Eu anomalies (Fig. 5c) could reflect the minor accumulation of plagioclase or removal of early-crystallized plagioclase during melt differentiation.

Overall, leucosomes in migmatites from the North Wulan gneiss complex show low concentrations of Y and HREE as well as high Sr/Y and $(La/Yb)_N$ ratios. These features are similar to those found in adakites (e.g. Defant and Drummond, 1990) and are usually interpreted to reflect anatexis of metabasic compositions at high-pressure granulite to eclogite facies conditions with garnet-rich and plagioclase-poor residues (Chung et al., 2003; Castillo, 2006; He et al., 2011). However, recent studies suggest that melt with low concentrations of Y and HREE and high Sr/Y and $(La/Yb)_N$ ratios can also be produced by water-fluxed melting of dioritic rocks at relatively low pressures in the middle crust (Slagstad et al., 2005; Reichardt and Weinberg, 2012; Wang et al., 2013; Hu et al., 2016). In addition, garnet is absent from

both leucosomes and melanosomes in migmatitic amphibole-biotite gneiss in the North Wulan gneiss complex, but amphibole is ubiquitous in the melanosome. Thus, the low concentrations of Y and HREE as well as high Sr/Y and $(La/Yb)_N$ ratios of leucosomes in migmatitic amphibole-biotite gneiss are likely attributed to the consumption of plagioclase during water-fluxed melting (e.g. Patiño Douce and Harris, 1998) and the growth of peritectic amphibole that partitions Y and HREE (e.g. Reichardt and Weinberg, 2012). The retention of amphibole and consumption of plagioclase during partial melting as well as the accumulation of plagioclase during fractional crystallization may jointly induce the 'adakitic' signature (e.g. Slagstad et al., 2005; Reichardt and Weinberg, 2012; Wang et al., 2013; Hu et al., 2016). In the case of the North Wulan gneiss complex, this signature is not directly related to melting of a subducting oceanic slab nor high-pressure melting of thickened or delaminated lower crust.

6.6. Tectonic history of the South Qilian–North Qaidam orogenic belt

The South Qilian–North Qaidam orogenic belt preserves a nearly complete history of the South Qilian ocean. The South Qilian accretionary belt records early-stage oceanic subduction and accretion of an intra-oceanic arc (Fu et al., 2014; Zhang et al., 2017; Song et al., 2017). By contrast, the North Qaidam HP–UHP metamorphic complex belt reflects continental subduction after the closure of the South Qilian ocean, which is characterized by UHP metamorphic gneisses, eclogites and garnet peridotites (Yang et al., 2006; Yu et al., 2013; Song et al., 2014a; Zhang et al., 2017). However, the protoliths of most eclogites are middle Neoproterozoic (850–750Ma) mafic igneous rocks that are interpreted to have formed in an intracontinental rift (Song et al., 2010; Xu et al., 2016). Some eclogites have early Paleozoic

protoliths that were subducted just before the onset of continental subduction (e.g. Song et al., 2006; Zhang et al., 2008). Thus, the North Qaidam HP–UHP metamorphic complex belt records a history from late-stage oceanic subduction to late-stage continental subduction and experienced multiple early Paleozoic metamorphic events (Zhang et al., 2013; Song et al., 2014a). Therefore, it is expected that multiple partial melting events accompanied the evolution of the South Qilian–North Qaidam orogenic belt.

Two mechanisms have been proposed to account for partial melting in South Qilian–North Qaidam orogenic belt: (1) HP granulite-facies partial melting of a thickened (>50 km) mafic lower crust (Yu et al., 2012, 2014, 2017b), and (2) decompression melting of eclogite during exhumation of subducted oceanic and continental crust from UHP conditions (Song et al., 2014b; Zhang et al., 2015; Yu et al., 2017a). The North Wulan gneiss complex was located in the hanging wall of the Paleozoic subduction system and migmatites in the complex formed by water-fluxed partial melting of a mafic to intermediate protolith at amphibolite-facies conditions without the generation of peritectic garnet. These features are incompatible with hydrate-breakdown melting that occurred in both the thickened mafic lower crust and the exhumed eclogite. Metamorphism and partial melting of HP granulite-facies rocks occurred between 438 and 432 Ma (Yu et al., 2014) whereas anatexis of the exhumed eclogite took place at 435–410 Ma (Song et al., 2014b). These events are significantly younger than the timing of anatexis in the North Wulan gneiss complex (465–450 Ma) (Figs. 9, 11). However, partial melting in the North Wulan gneiss complex temporally overlaps the metamorphic age of ocean-derived eclogite that is proposed to represent a metamorphosed ophiolite (460–440 Ma) (Song et al., 2006, 2014a; Zhang et al., 2008, 2009). Anatexis in the North Wulan gneiss complex is

also older than the continental subduction event (440–420 Ma) (Zhang et al., 2010), but it is coeval with continental arc magmatism in the South Qilian–North Qaidam orogenic belt (470–444 Ma) (Wu et al., 2009, 2014). Therefore, anatexis in the North Wulan gneiss complex is possibly the result of heat advected by continental arc magmatism.

The South Qilian–North Qaidam orogenic belt is bounded by the Qaidam Block to the southwest and the Qilian Block to the northeast (Fig. 1b). These two blocks have a similar tectonic evolution prior to the breakup of Rodinia (Li et al., 2008). After the breakup of the Rodinian supercontinent, the growth of the South Qilian ocean separated the Qilian Block from the Qaidam Block (Yang et al., 2006). The Oulongbuluke microcontinental block is another smaller-scale microcontinent fragment that has an older metamorphic basement than the Qaidam and Qilian Blocks (e.g. Chen et al., 2009, 2012). The Oulongbuluke microcontinental block was accreted to the south margin of the Qilian Block during early Paleozoic northward subduction of the South Qilian oceanic lithosphere, which resulted in an active continental arc setting (Xiao et al., 2009; Yan et al., 2012, 2015).

The North Wulan gneiss complex is located in the northeastern part of the Oulongbuluke microcontinental block in the hanging wall of an early Paleozoic subduction system. The North Wulan gneiss complex was subjected to high-temperature/low-pressure metamorphism (680–700°C at 3.5–4.2 kbar) at *ca.* 483–450 Ma (Li et al., 2015a). Gabbros with arc-like compositional signatures and zircon crystallization ages of 483–472 Ma are found in the North Wulan gneiss complex (our unpublished data), which indicates that underplating of mantle-derived magma was coeval with metamorphism and anatexis in the complex. Granitoid magmatism at *ca.* 464–440 Ma in the North Wulan gneiss complex (Sun et al., 2015) is also

coeval with anatexis. Thus, we propose that anatexis in the North Wulan gneiss complex resulted from magmatism generated during the northward subduction of South Qilian ocean (as a branch of Proto-Tethyan ocean) beneath the Qilian Block. Magmatic heating and fluid released by contemporaneous arc-related magmatism caused high-temperature–low-pressure metamorphism and anatexis in the North Wulan gneiss complex. Similar scenarios of high-temperature metamorphism and anatexis in arc settings have been reported in many orogenic belts, such as the Qinling Group in Qingling-Tongbai orogeny (Xiang et al., 2012), the Gangdese magmatic arc in the Himalaya (Zhang et al., 2013), and the southwestern Tianshan Migmatite Complex in the Central Asian Orogenic Belt (Xia et al., 2014).

7. Conclusions

A combination of fieldwork, petrography, whole-rock geochemistry, zircon U–Pb geochronology, and Hf isotope and trace elements analyses of zircon is used to investigate the timing and petrogenesis of gabbroic–dioritic migmatite in the North Wulan gneiss complex from the South Qilian–North Qaidam orogenic belt. Based on these results, we conclude:

(1) Migmatites formed by water-fluxed melting of mafic to intermediate rocks through the breakdown of biotite and growth of peritectic amphibole. Fractional crystallization of feldspar and accessory minerals (such as zircon, apatite and titanite) growth and dissolution had a significant influence on the concentrations of major and trace elements in leucosome.

(2) Zircon U–Pb geochronology reveals that the protolith of the migmatites crystallized at 506–494 Ma, and metamorphism and anatexis occurred at *ca.* 465 to 450 Ma. Zircon Hf isotope compositions demonstrate that new anatectic zircon rims grew in a relatively closed

isotopic system through dissolution–reprecipitation of pre-existing zircon.

(3) The protolith of the migmatites records Cambrian arc magmatism in an active continental margin. Anatexis likely took place in this continental arc setting, which reflects the reworking of Cambrian arc-like rocks in a late stage of the northward subduction of the South Qilian ocean slab.

Acknowledgements

We are grateful to Dr. Wei Zhang and Dr. Quanzhong Li for their assistance with SHRIMP and LA-ICP-MS zircon U–Pb dating, Dr. Jinhui Yang and Dr. Yueheng Yang for their help with zircon Lu–Hf isotope analyses, Chunlei Zong for her assistance with whole-rock major and trace elements analysis. We thank Prof. Dazhi Jiang, Dr. Qi Wu, Yu Han, Liangchao Da, Yusong Wang and Ting Wang for their field assistance. Fruitful comments and constructive evaluation by Prof. Shuguang Song and an anonymous reviewer resulted in improved version of this manuscript. We are also grateful to associate Editor Yunpeng Dong and Editor-in-chief M. Santosh for their comments and detailed editorial handing. This study was financially supported by the National Natural Science Foundation of China (41272221, 41372207, 41772228), the Key Program of the Ministry of Land and Resources of China (1212011120159, 12120115069401, DD20160022), and China Scholarship Council Scholarship Program (201606690007).

References

Andersson, J., Möller, C., Johansson, L., 2002. Zircon geochronology of migmatite gneisses along the Mylonite Zone (S Sweden): a major Sveconorwegian terrane boundary in the Baltic Shield. Precambrian Research 114, 121–147.

Annen, C., Sparks, R.S.J., 2002. Effects of repetitive emplacement of basaltic intrusions on thermal evolution and melt generation in the crust. Earth and Planetary Science Letters 203, 937–955.

Bea, F., Pereira, M.D., Stroh, A., 1994. Mineral/leucosome trace-element partitioning in a peraluminous migmatite (a laser ablation-ICP-MS study). Chemical Geology 117, 291–312.

Boynton, W.V., 1984. Cosmochemistry of the rare earth elements: meteorite studies. In: Henderson, P. (Eds.), Rare Earth Element Geochemistry. Elsevier, Amsterdam, 63–114.

Bröcker, M., Klemd, R., Kooijman, E., Jasper, B., Larionov, A., 2010. Zircon geochronology and trace element characteristics of eclogites and granulites from the Orlica–Snieznik complex, Bohemian Massif. Geological Magazine 147, 339–362.

Brown, C.R., Yakymchuk, C., Brown, M., Fanning, C.M., Korhonen, F.J., Piccoli, P.M., Siddoway, C.S., 2016. From Source to Sink: Petrogenesis of Cretaceous Anatectic Granites from the Fosdick Migmatite–Granite Complex, West Antarctica. Journal of Petrology 57, 1241–1278.

Brown, M., 2001. Crustal melting and granite magmatism: key issues. Physics and Chemistry of the Earth, Part A: Solid Earth and Geodesy 26, 201–212.

Brown, M., 2007. Crustal melting and melt extraction, ascent and emplacement in orogens: mechanisms and consequences. Journal of the Geological Society 164, 709–730.

Brown, M., 2010. Melting of the continental crust during orogenesis: the thermal, rheological, and compositional consequences of melt transport from lower to upper continental crust. Canadian. Journal of Earth Sciences 47, 655–694.

Brown, M., 2013. Granite: From genesis to emplacement. Geological Society of America Bulletin 125, 1079–1113.

Carvalho, B.B., Sawyer, E.W., Janasi, V.A., 2016. Crustal reworking in a shear zone: transformation of metagranite to migmatite. Journal of Metamorphic Geology 34, 237–264.

Castillo, P.R., 2006. An overview of adakite petrogenesis. Chinese Science Bulletin 51, 257–268.

Chen, N.S., Gong, S.L., Sun, M., Li, X.Y., Xia, X.P., Wang, Q.Y., Wu, F.Y., Xu, P., 2009. Precambrian evolution of the Quanji Block, northeastern margin of Tibet: insights from zircon U–Pb and Lu–Hf isotope compositions. Journal of Asian Earth Sciences 35, 367–376.

Chen, N.S., Zhang, L., Sun, M., Wang, Q.Y., Kusky, T.M., 2012. U–Pb and Hf isotopic compositions of detrital zircons from the paragneisses of the Quanji Massif, NW China: implications for its early tectonic evolutionary history. Journal of Asian Earth Sciences 54, 110–130.

Cheng, T.T., Niu, M.L., Wu, Q., Xia, W.J., Li, X.C., 2015. Petrogenesis of the Chahannuo gabbro on the northern margin of Qaidam Basin: Constraint from geochemistry, zircon U–Pb dating and Lu–Hf isotopes. Chinese Journal of Geology 50, 741–755 (in Chinese with English abstract).

Cherniak, D.J., Watson, E.B., 2003. Diffusion in zircon. Reviews in Mineralogy and

Geochemistry 53, 113–143.

Chung, S.L., Liu, D.Y., Ji, J.Q., Chu, M.F., Lee, H.Y., Wen, D.J., Lo, C.H., Lee, T.Y., Qian, Q., Zhang, Q., 2003. Adakites from continental collision zones: melting of thickened lower crust beneath southern Tibet. Geology 31, 1021–1024.

Clemens, J.D., Vielzeuf, D., 1987. Constraints in melting and magma production in the crust. Earth and Planetary Science Letters 86, 287–306.

Clemens, J.D., 2006. Melting of the continental crust: fluid regimes, melting reactions, and source-rock fertility In: Brown, M., Rushmer, T. (Eds.), Evolution and differentiation of the continental crust. Cambridge University Press, Cambridge, UK, 297–331

Clemens, J.D., Stevens, G., 2012. What controls chemical variation in granitic magmas? Lithos 134, 317–329.

Corfu, F., Noble, S.R., 1992. Genesis of the southern Abitibi greenstone belt, Superior Province, Canada: evidence from zircon Hf isotope analyses using a single filament technique. Geochimica et Cosmochimica Acta 56, 2081–2097.

Corfu, F., Hanchar, J.M., Hoskin, P.W., Kinny, P., 2003. Atlas of zircon textures. Reviews in Mineralogy and Geochemistry 53, 469–500.

Da, L.C., Niu, M.L., Li, X.C., Han, Y., Wu, Q., Yan, Z., Zhao, Q.Q., 2017. Tectonic deformation characteristics of the L tectonites in Erlangdong area at the northern margin of Qaidam basin and its geological significance. Chinese Journal of Geology 52, 1038–1057 (in Chinese with English abstract).

Defant, M.J., Drummond, M.S., 1990. Derivation of some modern arc magmas by melting of young subducted lithosphere. Nature 347, 662–665.

Flowerdew, M.J., Millar, I.L., Vaughan, A.P.M., Horstwood, M.S.A., Fanning, C.M., 2006. The source of granitic gneisses and migmatites in the Antarctic Peninsula: a combined U–Pb SHRIMP and laser ablation Hf isotope study of complex zircons. Contributions to Mineralogy and Petrology 151, 751–768.

Foster, D.A., Schafer, C., Fanning, C.M., 2001. Relationships between crustal partial melting, plutonism, orogeny, and exhumation: Idaho-Bitterroot batholith. Tectonophysics 342, 313–350.

Fraser, G., Ellis, D., Eggins, S., 1997. Zirconium abundance in granulite facies minerals, with implications for zircon geochronology in high grade rocks. Geology 25, 607–610.

Fu, C.L., Yan, Z., Guo, X.Q., Niu, M.L., Xia, W.J., Wang, Z.Q., Li, J.L., 2014. Geochemistry and SHRIMP zircon U–Pb age of diabases in the Lajishankou ophiolitic mélange, South Qilian terrane. Acta Petrologica Sinica 30, 1659–1706 (in Chinese with English abstract).

Genier, F., Bussy, F., Epard, J.L., Baumgartner, L., 2008. Water-assisted migmatization of metagraywackes in a Variscan shear zone, Aiguilles-Rouges massif, western Alps. Lithos 102, 575–597.

Gerdes, A., Zeh, A., 2009. Zircon formation versus zircon alteration—new insights from combined U–Pb and Lu–Hf in-situ LA-ICP-MS analyses, and consequences for the interpretation of Archean zircon from the Central Zone of the Limpopo Belt. Chemical Geology 261, 230–243.

Guo, A.L., Zhang, G.W., Qiang, J., Sun, Y.G., Li, G., Yao, A.P., 2009. Indosinian Zongwulong belt on the northeastern margin of the Qinghai-Tibet Plateau. Acta Petrologica Sinica 25, 1–12 (in Chinese with English abstract).

He, Y.S., Li, S.G., Hoefs, J., Huang, F., Liu, S.A., Hou, Z., 2011. Postcollisional granitoids from the Dabie orogen: new evidence for partial melting of a thickened continental crust. Geochimica et Cosmochimica Acta 75, 3815–3838.

Hu, Z.P., Zhang, Y.S., Hu, R., Wang, J., Siebel, W., Chen, F., 2016. Amphibole-bearing migmatite in North Dabie, eastern China: Water-fluxed melting of the orogenic crust. Journal of Asian Earth Sciences 125, 100–116.

Kang, Z., Jiang, C.Y., Ling, J.L., Zhao, Y.F., Song, Y.F., Zhou, W., 2015. Petrogenesis and ore genesis of the ilmenite-rich Kendelong mafic–ultramafic intrusion in Wulan, Qinghai. Acta Petrologica Sinica 31, 193–2210 (in Chinese with English abstract).

Kelsey, D.E., Clark, C., Hand, M., 2008. Thermobarometric modelling of zircon and monazite growth in melt-bearing systems: Examples using model metapelitic and metapsammitic granulites. Journal of Metamorphic Geology 26, 199–212.

Kelsey, D.E, Hand, M., 2015. On ultrahigh temperature crustal metamorphism: phase equilibria, trace element thermometry, bulk composition, heat sources, timescales and tectonic settings. Geoscience Frontiers 6, 311–356.

Lappin, A.R., Hollister, L.S., 1980. Partial melting in the Central Gneiss Complex near Prince Rupert, British Columbia. American Journal of Science 280, 518–545.

Lee, Y., Cho, M., 2013. Fluid-present disequilibrium melting in Neoarchean arc-related migmatites of Daeijak Island, western Gyeonggi Massif, Korea. Lithos 179, 249–262.

Li, X.C., Niu, M.L., Yan, Z., Da, L.C., Han, Y., Wang, Y.S., 2015a. LP/HT metamorphic rocks in Wulan County, Qinghai Province: An Early Paleozoic paired metamorphic belt on the northern Qaidam Basin?. Chinese Science Bulletin 60, 3501–3513 (in Chinese with English

abstract).

Li, X.C., Niu, M.L., Yan, Z., Wu, Q., Xia, W.J., Han, Y., Da, L.C., 2015b. SHRIMP Zircon dating for migmatitic biotite plagioclase gneiss from Erlangdong Dakendaban group in Wulan at the northern margin of Qaidam basin and its geological significant. Chinese Journal of Geology 50, 728–740 (in Chinese with English abstract).

Li, Z.X., Bogdanova, S.V., Collins, A.S., Davidson, A., De Waele, B., Ernst, R.E., Fitzsimons, I.C.W., Fuck, R.A., Gladkochub, D.P., Jacobs, J., Karlstrom, K.E., Lu, S.N., Natapov, L.M., Pease, V., Pisarevsky, S.A., Thrane, K., Vernikovsky, V., 2008. Assembly, configuration, and breakup history of Rodinia: a synthesis. Precambrian Research 160, 179–210.

Linnen, R.L., Keppler, H., 1997. Columbite solubility in granitic melts: consequences for the enrichment and fractionation of Nb and Ta in the earth's crust. Contributions to Mineralogy and Petrology 128, 213–227.

Lu, S.N., Yu, H.F., Li, H.K., Guo, K.Y., Wang, H.C., Jin, W., Zhang, C.L., Liu, Y.S., 2006. Research on Precambrian major problems in China. Geological Publishing Press, Beijing (in Chinese).

Morfin, S., Sawyer, E.W., Bandyayera, D., 2014. The geochemical signature of a felsic injection complex in the continental crust: Opinaca Subprovince, Quebec. Lithos 196, 339–355.

Palin, R.M., White, R.W., Green, E.C.R., Diener, J.F.A., Powell, R., Holland, T.J.B., 2016. High-grade metamorphism and partial melting of basic and intermediate rocks. Journal of Metamorphic Geology 34, 871–892.

Patiño Douce, A.E., Harris, N., 1998. Experimental constraints on Himalayan anatexis. Journal

of Petrology 39, 687–710.

Reichardt, H., Weinberg, R.F., 2012. Hornblende chemistry in meta-and diatexites and its retention in the source of leucogranites: an example from the Karakoram Shear Zone, NW India. Journal of Petrology 53, 1287–1318.

Rubatto, D., 2002. Zircon trace element geochemistry: partitioning with garnet and the link between U–Pb ages and metamorphism. Chemical Geology 184, 123–138.

Rubatto, D., Hermann, J., Berger, A., Engi, M., 2009. Protracted fluid-induced melting during Barrovian metamorphism in the Central Alps. Contributions to Mineralogy and Petrology 158, 703–722.

Sawyer, E.W., 1987. The role of partial melting and fractional crystallization in determining discordant migmatite leucosome compositions. Journal of Petrology 28, 445–473.

Sawyer, E.W., 2008. Atlas of migmatites. The Canadian Mineralogist Special Publication, NRC Research Press, Ottawa.

Sawyer, E.W., 2010. Migmatites formed by water-fluxed partial melting of a leucogranodiorite protolith: microstructures in the residual rocks and source of the fluid. Lithos 116, 273–286.

Schmidberger, S.S., Heaman, L.M., Simonetti, A., Creaser, R.A., Cookenboo, H.O., 2005. Formation of Paleoproterozoic eclogitic mantle, Slave Province (Canada): Insights from in-situ Hf and U–Pb isotopic analyses of mantle zircons. Earth and Planetary Science Letters 240, 621–633.

Shi, R.D., Yang, J.S., Wu, C.L., Tsuyoshi, L., Takafumi, H., 2006. Island arc volcanic rocks in the north Qaidam UHP belt, northern Tibet plateau: evidence for ocean–continent

subduction preceding continent–continent subduction. Journal of Asian Earth Sciences 28, 151–159.

Slagstad, T., Jamieson, R.A., Culshaw, N.G., 2005. Formation, crystallization, and migration of melt in the mid-orogenic crust: Muskoka domain migmatites, Grenville Province, Ontario. Journal of Petrology 46, 893–919.

Solar, G.S., Brown, M., 2001. Petrogenesis of migmatites in maine, USA: possible source of peraluminous leucogranite in plutons?. Journal of Petrology 42, 789–823.

Song, S.G., Zhang, L.F., Niu, Y.L., Su, L., Jian, P., Liu, D.Y., 2005. Geochronology of diamond-bearing zircons from garnet peridotite in the North Qaidam UHPM belt, Northern Tibetan Plateau: a record of complex histories from oceanic lithosphere subduction to continental collision. Earth and Planetary Science Letters 234, 99–118.

Song, S.G., Zhang, L.F., Niu, Y.L., Su, L., Song, B., Liu, D.Y., 2006. Evolution from oceanic subduction to continental collision: a case study from the Northern Tibetan Plateau based on geochemical and geochronological data. Journal of Petrology 47, 435–455.

Song, S.G., Su, L., Li, X.H., Zhang, G.B., Niu, Y.L., Zhang, L.F., 2010. Tracing the 850-Ma continental flood basalts from a piece of subducted continental crust in the North Qaidam UHPM belt, NW China. Precambrian Research 183, 805–816.

Song, S.G., Niu, Y.L., Su, L., Zhang, C., Zhang, L.F., 2014a. Continental orogenesis from ocean subduction, continent collision/subduction, to orogen collapse, and orogen recycling: The example of the North Qaidam UHPM belt, NW China. Earth-Science Reviews 129, 59–84.

Song, S.G., Niu, Y.L., Su, L., Wei, C.J., Zhang, L.F., 2014b. Adakitic (tonalitic-trondhjemitic)

magmas resulting from eclogite decompression and dehydration melting during exhumation in response to continental collision. Geochimica et Cosmochimica Acta 130, 42–62.

Song, S.G., Yang, L.M., Zhang, Y.Q., Niu, Y.L., Wang, C., Su, L., Gao, Y.L., 2017. Qi-Qin Accretionary Belt in Central China Orogen: accretion by trench jam of oceanic plateau and formation of intra-oceanic arc in the Early Paleozoic Qin-Qi-Kun Ocean. Science Bulletin 62, 1035–1038.

Storkey, A.C., Hermann, J., Hand, M., Buick, I.S., 2005. Using in situ trace-element determinations to monitor partial-melting processes in metabasites. Journal of Petrology 46, 1283–1308.

Sun, J.P., Chen, S.Y., Peng, Y., Shao, P.C., Ma, S., Liu, J., 2015. Determination of Early Cambrian Zircon SHRIMP U–Pb Datings in Zongwulong Tectonic Belt, Northern Margin of Qaidam Basin, and Its Geological Significance. Geological Review 61, 743–751 (in Chinese with English abstract).

Sun, S.S., McDonough, W.F., 1989. Chemical and isotopic systematic of ocean basalts: implicationsfor mantle composition and process. In: Saunders, A.D., Norry, M.J. (Eds.), Magmatism in the Ocean Basins. Geological Society of London vol. 42, 313–345.

Tang, M., Wang, X.L., Shu, X.J., Wang, D., Yang, T., Gopon, P., 2014. Hafnium isotopic heterogeneity in zircons from granitic rocks: Geochemical evaluation and modeling of "zircon effect" in crustal anatexis. Earth and Planetary Science Letters 389, 188–199.

Thompson, A.B., 1982. Dehydration melting of pelitic rocks and the generation of H_2O-undersaturated liquids. American Journal of Science 282, 1567–1595.

Vanderhaeghe, O., Teyssier, C., 2001. Partial melting and flow of orogens. Tectonophysics 342, 451–472.

Vielzeuf, D., Clemens, J.D., Pin, C., Moinet, E., 1990. Granites, granulites and crustal differentiation. In: Vielzeuf, D., Vidal, P. (Eds.), Granulites and Crustal Evolution. Kluwer, Dordrecht, Netherlands, 59–85.

Wallace, P.J., 2005. Volatiles in subduction zone magmas: concentrations and fluxes based on melt inclusion and volcanic gas data. Journal of Volcanology and Geothermal Research 140, 217–40.

Wang, L., Wang, H., He, C., Chen, N.S., Santosh, M., Sun, M., Wang, Q.Y., Jin, L.L., Liao, F.X., 2016. Mesoproterozoic continental breakup in NW China: Evidence from gray gneisses from the North Wulan terrane. Precambrian Research 281, 521–536.

Wang, Q.Y., Pan, Y.M., Chen, N.S., Li, X.Y., Chen, H.H., 2009. Proterozoic polymetamorphism in the Quanji Block, northwestern China: evidence from microtextures, garnet compositions and monazite CHIME ages. Journal of Asian Earth Sciences 34, 686–698.

Wang, S.J., Li, S.G., Chen, L.J., He, Y.S., An, S.C., Shen, J., 2013. Geochronology and geochemistry of leucosomes in the North Dabie Terrane, East China: implication for post-UHPM crustal melting during exhumation. Contributions to Mineralogy and Petrology 165, 1009–1029.

Watkins, J.M., Clemens, J.D., Treloar, P.J., 2007. Archaean TTGs as sources of younger granitic magmas: melting of sodic metatonalites at 0.6–1.2 GPa. Contributions to Mineralogy and Petrology 154, 91–110.

Watt, G.R., Harley, S.L. 1993. Accessory phase controls on the geochemistry of crustal melts and restites produced during water-undersaturated partial melting. Contributions to Mineralogy and Petrology 114, 550–566.

Weinberg, R.F., Hasalová, P., 2015. Water-fluxed melting of the continental crust: A review. Lithos 212, 158–188.

Whitney, D.L., Irving, A.J., 1994. Origin of K-poor leucosomes in a metasedimentary migmatite complex by ultrametamorphism, syn-metamorphic magmatism and subsolidus processes. Lithos 32, 173–192.

Whitney, D.L., Evans, B.W., 2010. Abbreviations for names of rock-forming minerals. American mineralogist 95, 185–187.

Wickham, S.M., Oxburgh, E.R., 1987. Low-pressure metamorphism in the Pyrenees and its implications for the thermal evolution of rifted continental crust. Philosophical Transactions of the Royal Society of London A: Mathematical, Physical and Engineering Sciences 321, 219–242.

Williams, I.S., 2001. Response of detrital zircon and monazite, andtheir U–Pb isotopic systems, to regional metamorphism and host-rock partial melting, Cooma Complex, southeastern Australia. Australian Journal of Earth Sciences 48, 557–580.

Wu, C.L., Wooden, J.L., Robinson, P.T., Gao, Y.H., Wu, S.P., Chen, Q.L., Mazdab, F.K., Mattinson, C., 2009. Geochemistry and zircon shrimp U–Pb dating of granitoids from the west segment of the North Qaidam. Science in China Series D: Earth Sciences 52, 1771–1790.

Wu, C.L., Gao, Y.H., Li, Z.L., Lei, M., Qin, H.P., Li, M.Z., Liu, C.H., Frost, R.B., Robinson,

P.T., Wooden, J.L., 2014. Zircon SHRIMP U–Pb dating of granites from Dulan and the chronological framework of the North Qaidam UHP belt, NW China. Science China: Earth Sciences 44, 2142–2159.

Wu, Y.B., Zheng, Y.F., Zhang, S.B., Zhao, Z.F., Wu, F.Y., Liu, X.M., 2007. Zircon U–Pb ages and Hf isotope compositions of migmatite from the North Dabie terrane in China: constraints on partial melting. Journal of Metamorphic Geology 25, 991–1009.

Xia, B., Zhang, L.F., Bader, T., 2014. Zircon U–Pb ages and Hf isotopic analyses of migmatite from the 'paired metamorphic belt' in Chinese SW Tianshan: constraints on partial melting associated with orogeny. Lithos 192, 158–179.

Xiang, H., Zhang, L., Zhong, Z.Q., Santosh, M., Zhou, H.W., Zhang, H.F., Zheng, J.P., Zheng, S., 2012. Ultrahigh-temperature metamorphism and anticlockwise P-T-t path of Paleozoic granulites from north Qinling-Tongbai orogen, Central China. Gondwana Research 21, 559–576.

Xiao, W.J., Windley, B.F., Yong, Y., Yan, Z., Yuan, C., Liu, C.Z., Li, J.L., 2009. Early Paleozoic to Devonian multiple-accretionary model for the Qilian Shan, NW China. Journal of Asian Earth Sciences 35, 323–333.

Xu, X., Song, S.G., Allen, M.B., Ernst, R.E., Niu, Y.L., Su, L., 2016. An 850-820 Ma LIP dismembered during breakup of the Rodinia supercontinent and destroyed by Early Paleozoic continental subduction in the northern Tibetan Plateau, NW China. Precambrian Research 282, 52-73.

Yakymchuk, C., Brown, M., 2014. Behaviour of zircon and monazite during crustal melting. Journal of the Geological Society 171, 465–479.

Yakymchuk, C., Brown, C.R., Brown, M., Siddoway, C.S., Fanning, C.M., Korhonen, F.J., 2015. Paleozoic evolution of western Marie Byrd Land, Antarctica. Geological Society of America Bulletin 127, 1464–1484.

Yakymchuk, C., Clark, C., White, R.W., 2017. Phase relations, reaction sequences and petrochronology. Reviews in Mineralogy and Geochemistry 83, 13–53.

Yakymchuk, C., Kirkland, C.L., Clark, C., 2018. Th/U ratios in metamorphic zircon. Journal of Metamorphic Geology, doi: 10.1111/jmg.12307.

Yan, Z., Wang, Z.Q., Li, J.L., Xu, Z.Q., Deng, J.F., 2012. Tectonic settings and accretionary orogenesis of the West Qinling Terrane, northeastern margin of the Tibet Plateau. Acta Petrologica Sinica 28, 1808–1828 (in Chinese with English abstract).

Yan, Z., Aitchison, J., Fu, C.L., Guo, X.Q., Niu, M.L., Xia, W.J., Li, J.L., 2015. Hualong Complex, South Qilian terrane: U–Pb and Lu–Hf constraints on Neoproterozoic micro-continental fragments accreted to the northern Proto-Tethyan margin. Precambrian Research 266, 65–85.

Yang, J.S., Wu, C.L., Zhang, J.X., Shi, R.D., Meng, F.C., Wooden, J., Yang, H.Y., 2006. Protolith of eclogites in the north Qaidam and Altun UHP terrane, NW China: earlier oceanic crust?. Journal of Asian Earth Sciences 28, 185–204.

Yardley, B.W.D., Valley, J.W., 1997. The petrologic case for a dry lower crust. Journal of Geophysical Research: Solid Earth 102, 12173–12185.

Yu, F.C., Wei, G.F., Sun, J.D., 1994. The Pattern of Mineralization of Gold Deposit SynTectonics in Dark Rock Series: By Tanjianshan Gold Deposit. The Publishing House of Northwest University, Xi'an (in Chinese with English abstract).

Yu, S.Y., Zhang, J.X., Del Real, P.G., 2012. Geochemistry and zircon U–Pb ages of adakitic rocks from the Dulan area of the North Qaidam UHP terrane, north Tibet: constraints on the timing and nature of regional tectonothermal events associated with collisional orogeny. Gondwana Research 21, 167–179.

Yu, S.Y., Zhang, J.X., Li, H.K., Hou, K.J., Mattinson, C.G., Gong, J.H., 2013. Geochemistry, zircon U Pb geochronology and Lu Hf isotopic composition of eclogites and their host gneisses in the Dulan area, North Qaidam UHP terrane: New evidence for deep continental subduction. Gondwana Research 23, 901–919.

Yu, S.Y., Zhang, J.X., Mattinson, C.G., Del Real, P.G., Li, Y.S., Gong, J.H., 2014. Paleozoic HP granulite-facies metamorphism and anatexis in the Dulan area of the North Qaidam UHP terrane, western China: constraints from petrology, zircon U–Pb and amphibole Ar–Ar geochronology. Lithos 198, 58–76.

Yu, S.Y., Zhang, J.X., Sun, D.Y., Li, Y.S., Gong, J.H, 2015. Anatexis of ultrahigh-pressure eclogite during exhumation in the North Qaidam ultrahigh-pressure terrane: Constraints from petrology, zircon U–Pb dating, and geochemistry. Geological Society of America Bulletin 127, 1290–1312.

Yu, S.Y., Zhang, J.X., Li, S.Z., Peng Y.B., 2017a. Anatexis, Deformation and Exhumation Mechanism for UHP Metamorphic Rocks: A Case Study in the North Qaidam and South Altyn UHP terrane, Western China. Acta Geologica Sinica 91, 361–362.

Yu, S.Y., Li, S.Z., Zhang, J.X., Sun, D.Y., 2017b. Adakitic Rocks Resulting from Partial Melting of Metabasite at High-Pressure Granulite-Facies Condition during Continental Collision. Acta Geologica Sinica 91, 1157–1158.

Yu, S.Y., Zhang, J.X., Li, S.Z., Sun, D.Y., Li, Y.S., Liu, X., Guo, L.L., Suo, Y.H., Peng, Y.B., Zhao, X.L., 2017c. Paleoproterozoic granulite-facies metamorphism and anatexis in the Oulongbuluke Block, NW China: Respond to assembly of the Columbia supercontinent. Precambrian Research 291, 42–62.

Zeng, L.S., Asimow, P.D., Saleeby, J.B., 2005. Coupling of anatectic reactions and dissolution of accessory phases and the Sr and Nd isotope systematics of anatectic melts from a metasedimentary source. Geochimica et Cosmochimica Acta 69, 3671–3682.

Zhang, G.B., Song, S.G., Zhang, L.F., Niu, Y.L., 2008. The subducted oceanic crust within continental-type UHP metamorphic belt in the North Qaidam, NW China: evidence from petrology, geochemistry and geochronology. Lithos 104, 99–118.

Zhang, G.B., Zhang, L.F., Song, S.G., Niu, Y.L., 2009. UHP metamorphic evolution and SHRIMP geochronology of a coesite-bearing meta-ophiolitic gabbro in the North Qaidam, NW China. Journal of Asian Earth Sciences 35, 310–322.

Zhang, G.B., Zhang, L.F., Christy, A.G., 2013. From oceanic subduction to continental collision: an overview of HP–UHP metamorphic rocks in the North Qaidam UHP belt, NW China. Journal of Asian Earth Sciences 63, 98–111.

Zhang, J.X., Yang, J.S., Mattinson, C.G., Xu, Z.Q., Meng, F.C., Shi, R.D., 2005. Two contrasting eclogite cooling histories, North Qaidam HP/UHP terrane, western China: petrological and isotopic constraints. Lithos 84, 51–76.

Zhang, J.X., Mattinson, C.G., Yu, S.Y., Li, J.P., Meng, F.C., 2010. U–Pb zircon geochronology of coesite-bearing eclogites from the southern Dulan area of the North Qaidam UHP terrane, northwestern China: spatially and temporally extensive UHP metamorphism during

continental subduction. Journal of Metamorphic Geology 28, 955–978.

Zhang, J.X., Yu, S.Y., Mattinson, C.G., 2017. Early Paleozoic polyphase metamorphism in northern Tibet, China. Gondwana Research 41, 267–289.

Zhang, L., Chen, R.X., Zheng, Y.F., Hu, Z., 2015. Partial melting of deeply subducted continental crust during exhumation: insights from felsic veins and host UHP metamorphic rocks in North Qaidam, northern Tibet. Journal of Metamorphic Geology 33, 671–694.

Zhang, Y.Q., Song, S.G., Yang, L.M., Su, L., Niu, Y.L., Allen, M.B., Xu, X., 2017. Basalts and picrites from a plume-type ophiolite in the South Qilian Accretionary Belt, Qilian Orogen: Accretion of a Cambrian Oceanic Plateau?. Lithos 278, 97–110.

Zhang, Z.M., Dong, X., Xiang, H., Liou, J.G., Santosh, M., 2013. Building of the deep Gangdese arc, south Tibet: Paleocene plutonism and granulite-facies metamorphism. Journal of Petrology 54, 2547–2580.

Zheng, Y.F., Zhao, Z.F., Wu, Y.B., Zhang, S.B., Liu, X.M., Wu, F.Y., 2006. Zircon U–Pb age, Hf and O isotope constraints on protolith origin of ultrahigh-pressure eclogite and gneiss in the Dabie orogen. Chemical Geology 231, 135–158.

Figure captions

Fig. 1. (a) Tectonic framework of China and location of the study area. (b) Schematic map of the South Qilian–North Qaidam orogenic belt (modified after Zhang et al. 2005). (c) Geological map of the North Wulan gneiss complex showing sample locations.

Fig. 2. Photographs of migmatites from the North Wulan gneiss complex. (a) Gabbroic–dioritic migmatite in contact with metasandstone by a thrust fault. The metasandstone around the fault is folded. (b) Gabbroic–dioritic migmatite consisting of amphibole-biotite gneiss, melanosome and leucosome. (c) Melanosomes are located along the leucosome margin or within leucosome. (d) Stromatic leucosomes are parallel to the regional foliation (S_1). (e) Isoclinally folded leucosome. (f) Leucosome that is discordant to the dominant foliation (S_1). (g) Anastomosing network of leucosome in migmatite. (h) Small and irregular leucosome patch with coarse-grained amphibole in amphibole-biotite gneiss.

Fig. 3. Microstructures of migmatites from the North Wulan gneiss complex. (a) Amphibole-biotite gneiss with a mineral assemblage of amphibole, plagioclase, biotite and quartz, with the accessory ilmenite, zircon, and titanite. Biotite has irregular margins and locally forms clusters. (b) Relatively coarse-grained amphibole with rounded inclusions of plagioclase, minor quartz and biotite in amphibole-biotite gneiss. (c) Coarse-grained plagioclase with inclusions of plagioclase, quartz, biotite, amphibole and clinopyroxene in amphibole-biotite gneiss. (d) Irregularly polymineral inclusion consisting of biotite, quartz and plagioclase within coarse-grain plagioclase in amphibole-biotite gneiss. (e) Irregular cuspate feldspar and quartz grains occur along boundaries of biotite and amphibole. (f) Anhedral and corroded

clinopyroxene as inclusions in amphibole. (g) Biotite with corroded margins in leucosome. (h) The framework structure of subhedral to euhedral plagioclase crystals with interstitial K-feldspar and quartz in leucosome.

Fig. 4. Variation diagrams showing the compositions of migmatites in the North Wulan gneiss complex compared with dioritic migmatites from other migmatite terranes. Data for dioritic migmatites are from Slagstad et al. (2005), Reichardt and Weinberg (2012), Wang et al. (2013), and Hu et al. (2016).

Fig. 5. Chondrite-normalized REE patterns (a) and primitive mantle-normalized trace element patterns (b) for amphibole-biotite gneisses and melanosomes from the North Wulan gneiss complex. Chondrite-normalized REE patterns (c) and primitive-mantle normalized trace element patterns (d) for leucosomes within the amphibole-biotite gneisses. Chondrite values are from Boynton (1984). Primitive mantle values are from Sun and McDonough (1989).

Fig. 6. Variation diagrams of major oxide and trace element data for leucosomes in the North Wulan gneiss complex. Samples are divided into different groups based on their REE patterns. FeO^T represents total ferrous iron. Oxides are plotted as weight percent. Trace element concentrations are plotted as parts per million (ppm). Arrows with mineral labels point to the composition of that mineral. Single arrows represent the general trend of the data.

Fig. 7. Trace element variation diagrams for leucosomes in the North Wulan gneiss complex. Trace element concentrations are plotted as parts per million (ppm). Single arrows represent the general trend of the data.

Fig. 8. Representative CL images of zircons from samples 11RLD07 (a), 11RLD12 (b), 11RLD19 (c), 11RLD20 (d), 11RLD10 (e), 11RLD18 (f). The smaller circles with solid line show the locations of SHRIMP analyses and corresponding individual $^{206}Pb/^{238}U$ ages (above the analysis spots); the larger circles with the dashed lines mark locations of Lu–Hf isotope analysis and corresponding $\varepsilon Hf_{(t)}$ values (below the analysis spots). The white bars are 100 μm in length. U–Pb dates of samples 11RLD10 and 11RLD18 are from Li et al. (2015b).

Fig. 9. Concordia diagrams for SHRIMP zircon U–Pb analyses of samples 11RLD07 (a), 11RLD12 (b), 11RLD19 (c), 11RLD20 (d).

Fig. 10. Representative CL images of zircons from amphibole-biotite gneiss samples 12ELH4 (a) and 12ELH15 (b), and leucosome samples 12ELH3 (c), 12ELH5 (d), 12ELH12 (e) and 12ELH14 (f). The circles with solid line show the locations of LA-ICP-MS analyses and corresponding individual $^{206}Pb/^{238}U$ ages (above the analysis spots); the circles with dashed lines mark the locations of Lu–Hf isotope analysis and corresponding $\varepsilon Hf_{(t)}$ values (below the analysis spots). The white bars are 100 μm in length.

Fig. 11. Concordia diagrams of LA-ICP-MS zircon U–Pb analyses for amphibole-biotite gneiss samples 12ELH4 (a) and 12ELH15 (b), and leucosome samples 12ELH3 (c), 12ELH5 (d), 12ELH12 (e) and 12ELH14 (f). Data-point error ellipses are at 2σ confidence. Age uncertainties are reported at 95% confidence.

Fig. 12. Chondrite-normalized REE patterns for zircon from amphibole-biotite gneisses samples 12ELH4 (a) and 12ELH15 (b), and leucosome samples 12ELH3 (c), 12ELH5 (d), 12ELH12 (e) and 12ELH14 (f) in the North Wulan gneiss complex. Chondrite values are

from Boynton (1984).

Fig. 13. ($^{176}Hf/^{177}Hf$) initial vs. $^{176}Lu/^{177}Hf$, ($^{176}Hf/^{177}Hf$) initial vs. $^{206}Pb/^{238}U$ age, $\varepsilon Hf_{(t)}$ v. $^{176}Lu/^{177}Hf$, $\varepsilon Hf_{(t)}$ vs. $^{206}Pb/^{238}U$ age plots of zircons from amphibole-biotite gneisses and leucosomes in the North Wulan gneiss complex. Note that only the data from spots <520 Ma are plotted for the leucosome sample 11RLD12.

Highlights

Former arc magmatic rocks were reworked during late-stage oceanic subduction.

Anatexis occurred through the breakdown of biotite and growth of peritectic amphibole.

Water-fluxed melting took place in a relatively closed Hf isotopic system.

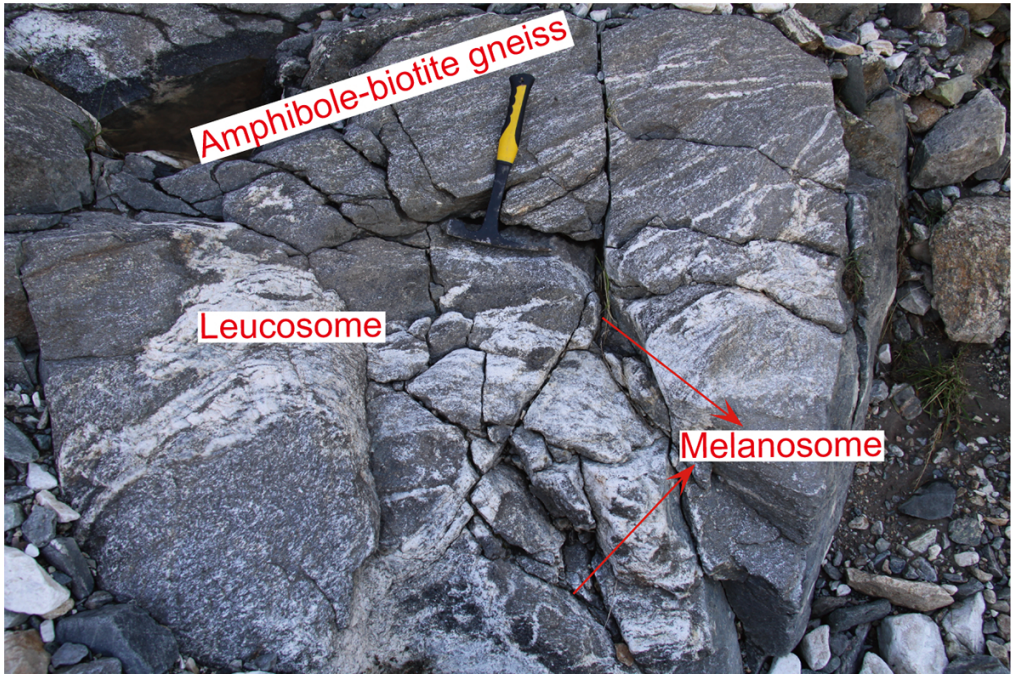

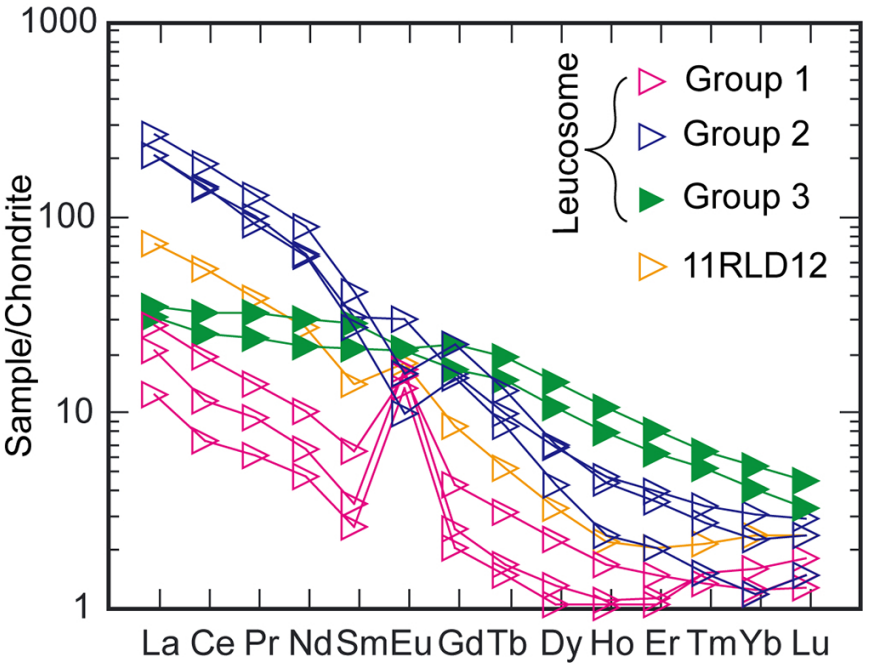

Graphics Abstract

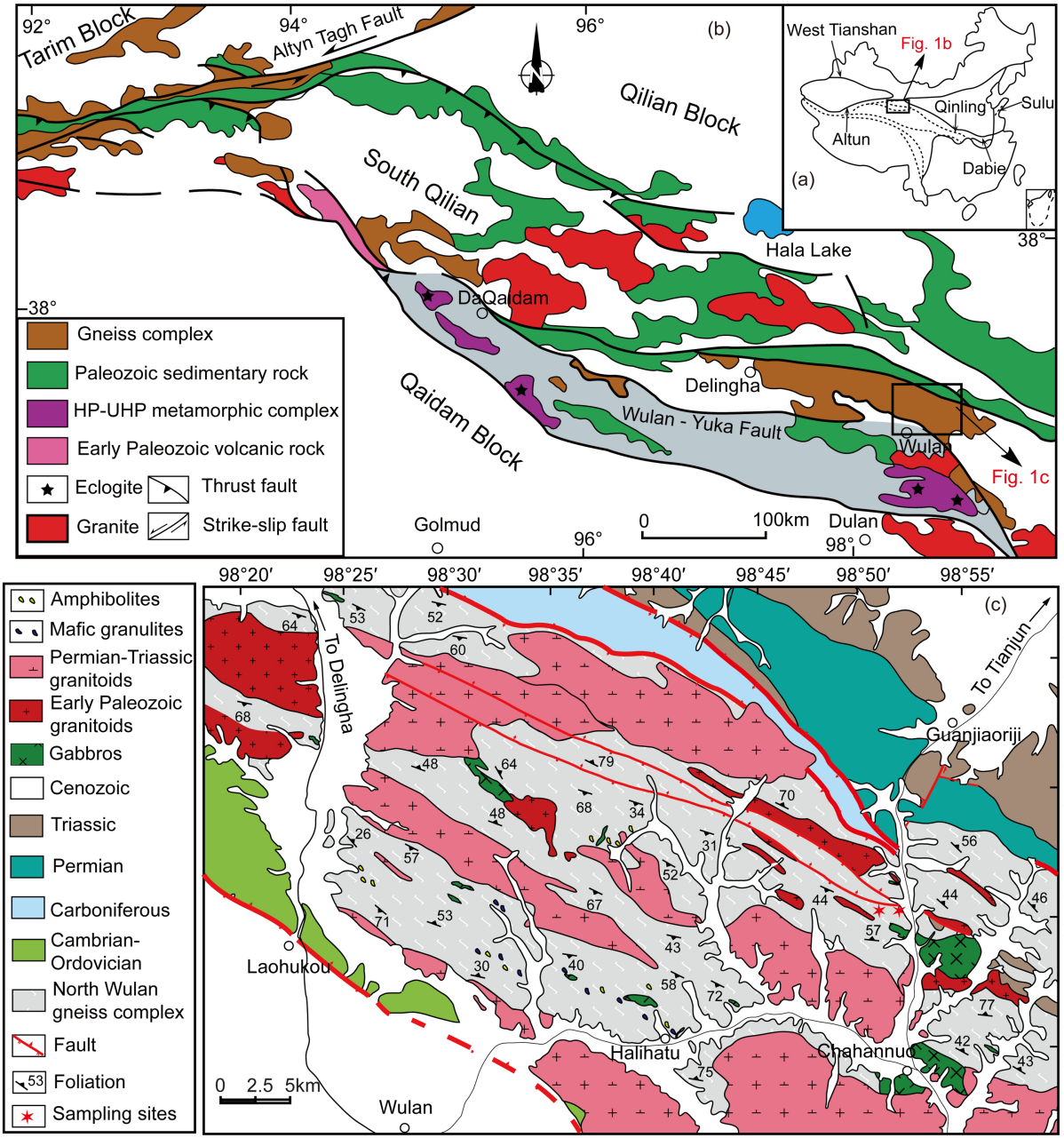
92°
94°
96°
Tarim Block
Altyn Tagh Fault
Qilian Block
South Qilian
Qaidam Block
Wulan - Yuka Fault
Hala Lake
DaQaidam
Delingha
Wulan
Golmud
Dulan
38°
0
100km
(b)
Fig. 1c
West Tianshan
Fig. 1b
Qinling
Sulu
Altun
Dabie
(a)
Gneiss complex
Paleozoic sedimentary rock
HP-UHP metamorphic complex
Early Paleozoic volcanic rock
Eclogite
Thrust fault
Granite
Strike-slip fault
98°20′
98°25′
98°30′
98°35′
98°40′
98°45′
98°50′
98°55′
37°15′
37°10′
37°05′
37°00′
(c)
To Delingha
To Tianjun
Guanjiaoriji
Laohukou
Halihatu
Chahannuo
Wulan
0 2.5 5km
Amphibolites
Mafic granulites
Permian-Triassic granitoids
Early Paleozoic granitoids
Gabbros
Cenozoic
Triassic
Permian
Carboniferous
Cambrian-Ordovician
North Wulan gneiss complex
Fault
Foliation
Sampling sites

Figure 1

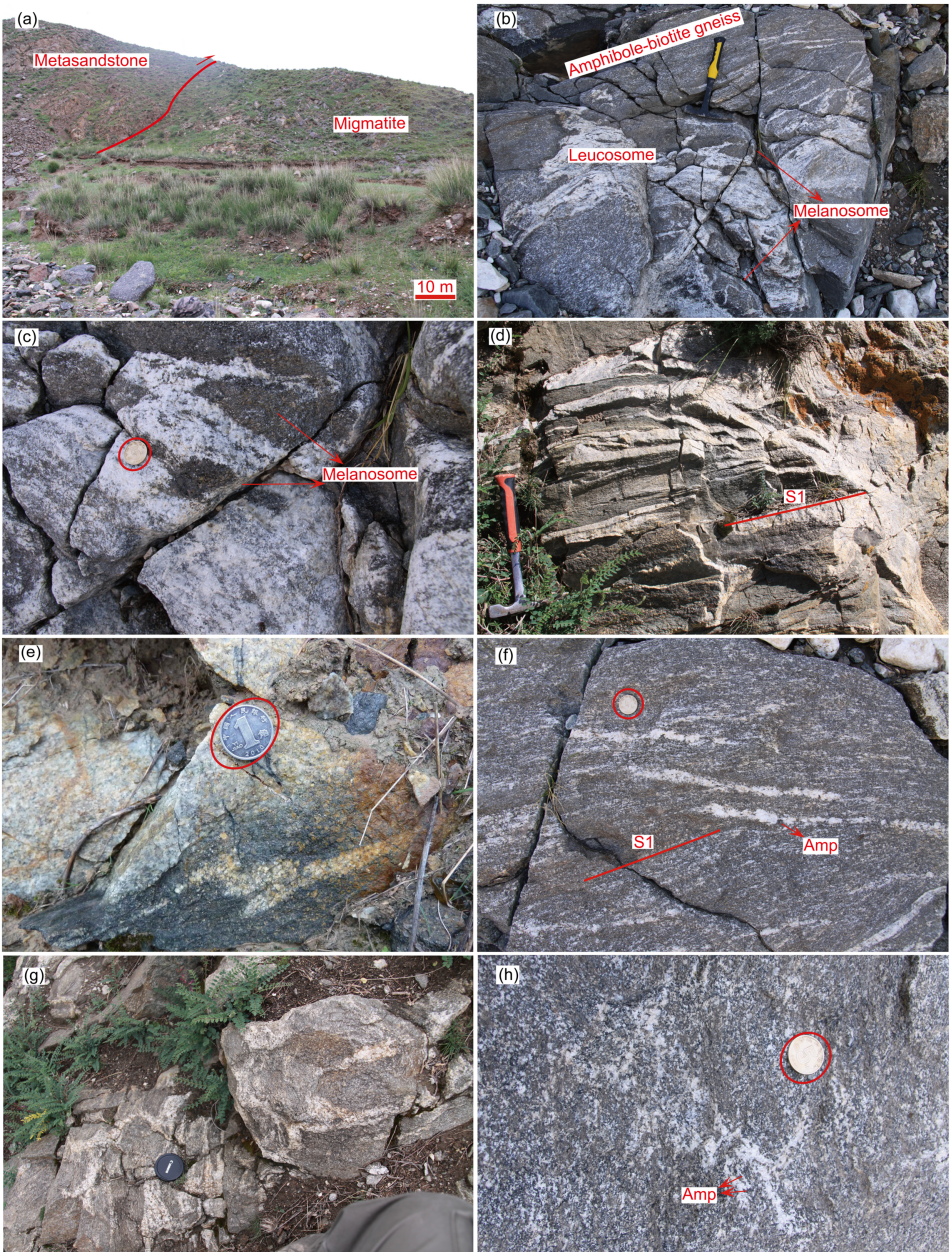
(a)
Metasandstone
Migmatite
10 m
(b)
Amphibole-biotite gneiss
Leucosome
Melanosome
(c)
Melanosome
(d)
S1
(e)
(f)
S1
Amp
(g)
(h)
Amp

Figure 2

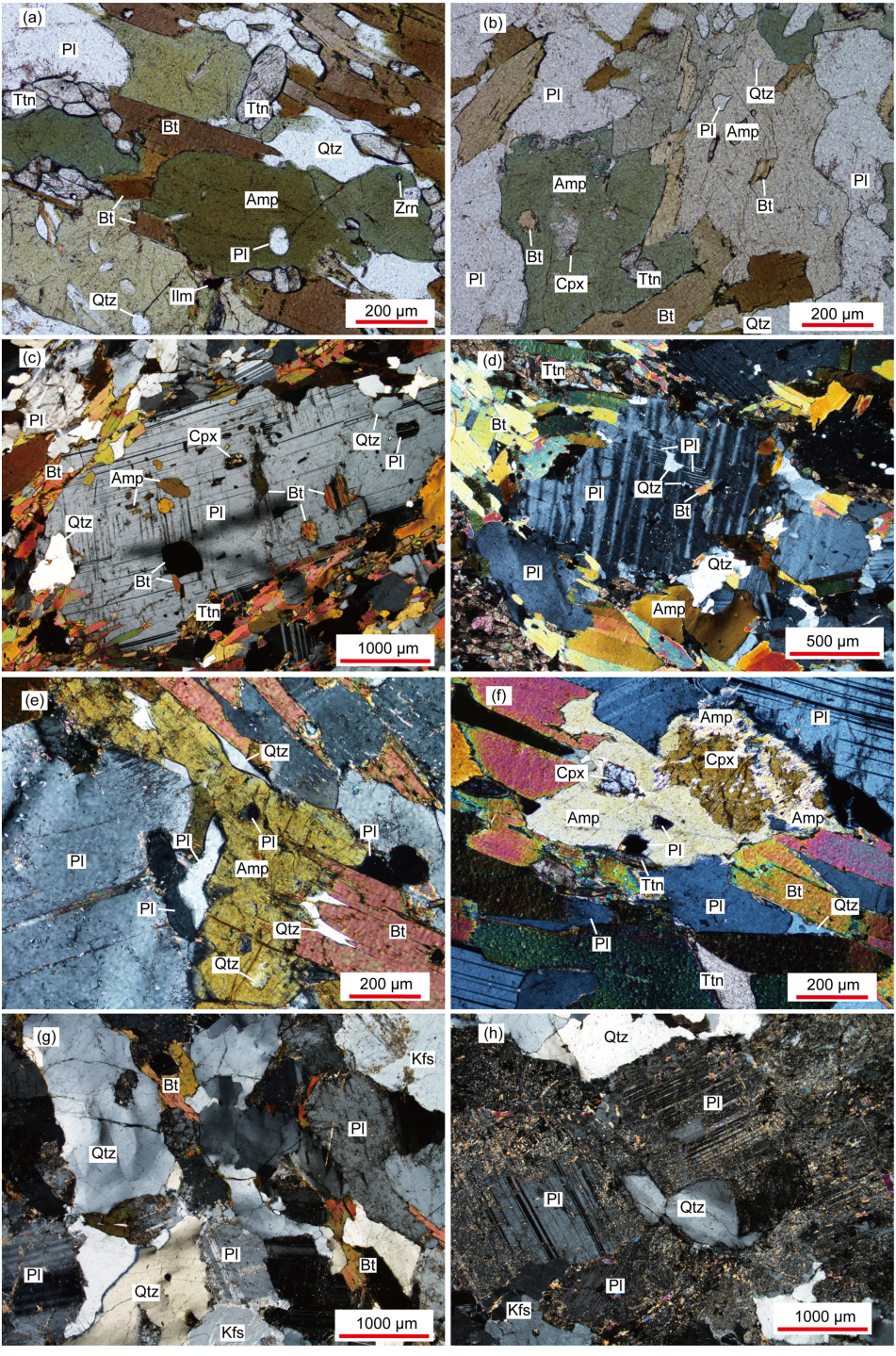
(a)
Pl
Ttn
Ttn
Bt
Qtz
Amp
Zrn
Bt
Pl
Qtz
Ilm
200 µm
(b)
Pl
Qtz
Pl
Amp
Amp
Pl
Bt
Bt
Pl
Cpx
Ttn
Bt
Qtz
200 µm
(c)
Pl
Cpx
Qtz
Pl
Bt
Amp
Bt
Qtz
Pl
Bt
Ttn
1000 µm
(d)
Ttn
Bt
Pl
Pl
Qtz
Bt
Pl
Qtz
Amp
500 µm
(e)
Qtz
Pl
Pl
Pl
Pl
Amp
Pl
Qtz
Bt
Qtz
200 µm
(f)
Amp
Pl
Cpx
Cpx
Amp
Amp
Pl
Ttn
Bt
Pl
Qtz
Pl
Ttn
200 µm
(g)
Kfs
Bt
Pl
Qtz
Pl
Pl
Bt
Qtz
Kfs
1000 µm
(h)
Qtz
Pl
Pl
Qtz
Pl
Kfs
1000 µm

Figure 3

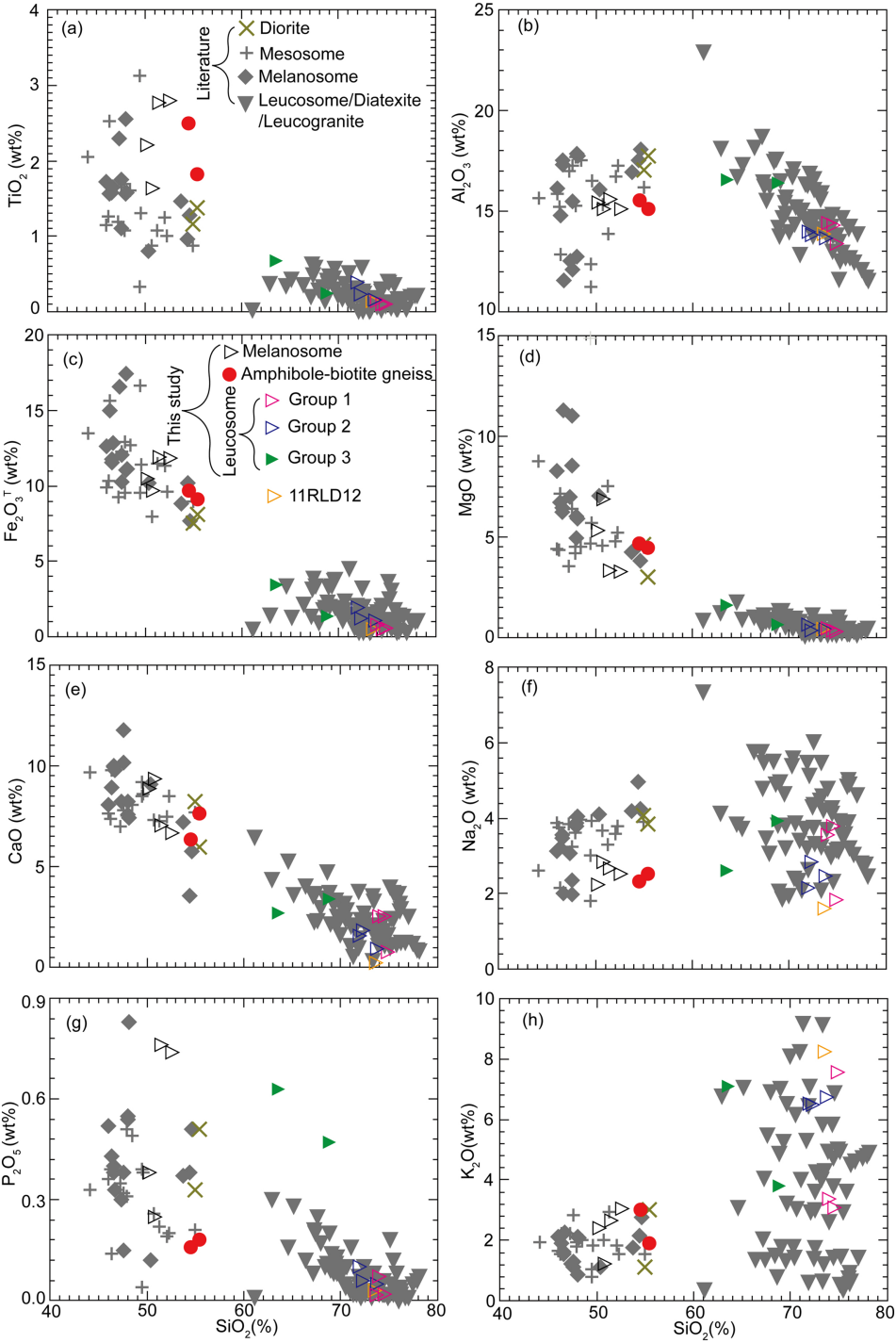
(a)
Literature
Diorite
Mesosome
Melanosome
Leucosome/Diatexite
/Leucogranite
TiO2 (wt%)
(b)
Al2O3 (wt%)
(c)
This study
Melanosome
Amphibole-biotite gneiss
Leucosome
Group 1
Group 2
Group 3
11RLD12
Fe2O3T (wt%)
(d)
MgO (wt%)
(e)
CaO (wt%)
(f)
Na2O (wt%)
(g)
P2O5 (wt%)
(h)
K2O(wt%)
SiO2(%)
SiO2(%)

Figure 4

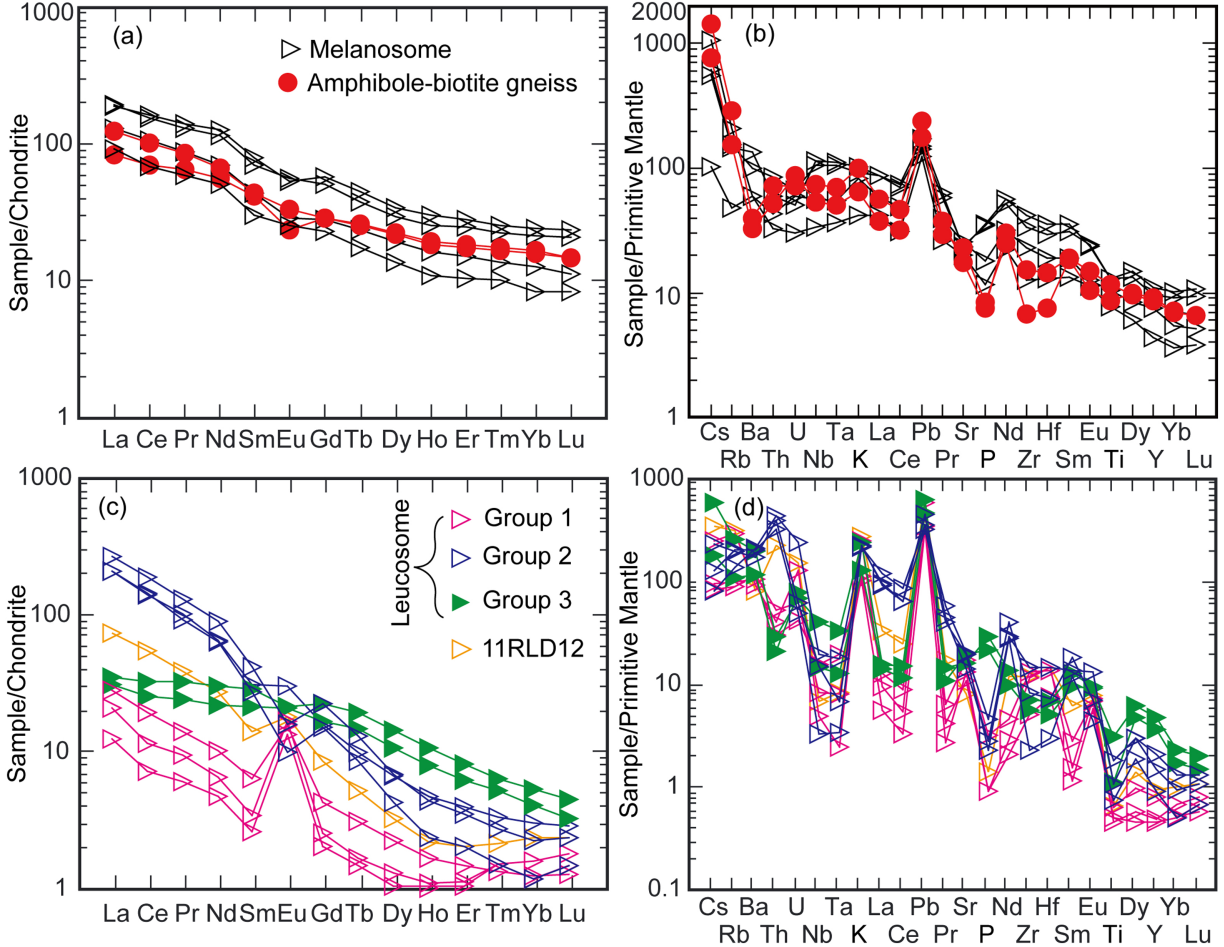
(a)
Melanosome
Amphibole-biotite gneiss
Sample/Chondrite
1000
100
10
1
La Ce Pr Nd Sm Eu Gd Tb Dy Ho Er Tm Yb Lu
(b)
Sample/Primitive Mantle
2000
1000
100
10
1
Cs Rb Ba Th U Nb Ta K La Ce Pb Pr Sr P Nd Zr Hf Sm Eu Ti Dy Y Yb Lu
(c)
Leucosome
Group 1
Group 2
Group 3
11RLD12
Sample/Chondrite
1000
100
10
1
La Ce Pr Nd Sm Eu Gd Tb Dy Ho Er Tm Yb Lu
(d)
Sample/Primitive Mantle
1000
100
10
1
0.1
Cs Rb Ba Th U Nb Ta K La Ce Pb Pr Sr P Nd Zr Hf Sm Eu Ti Dy Y Yb Lu

Figure 5

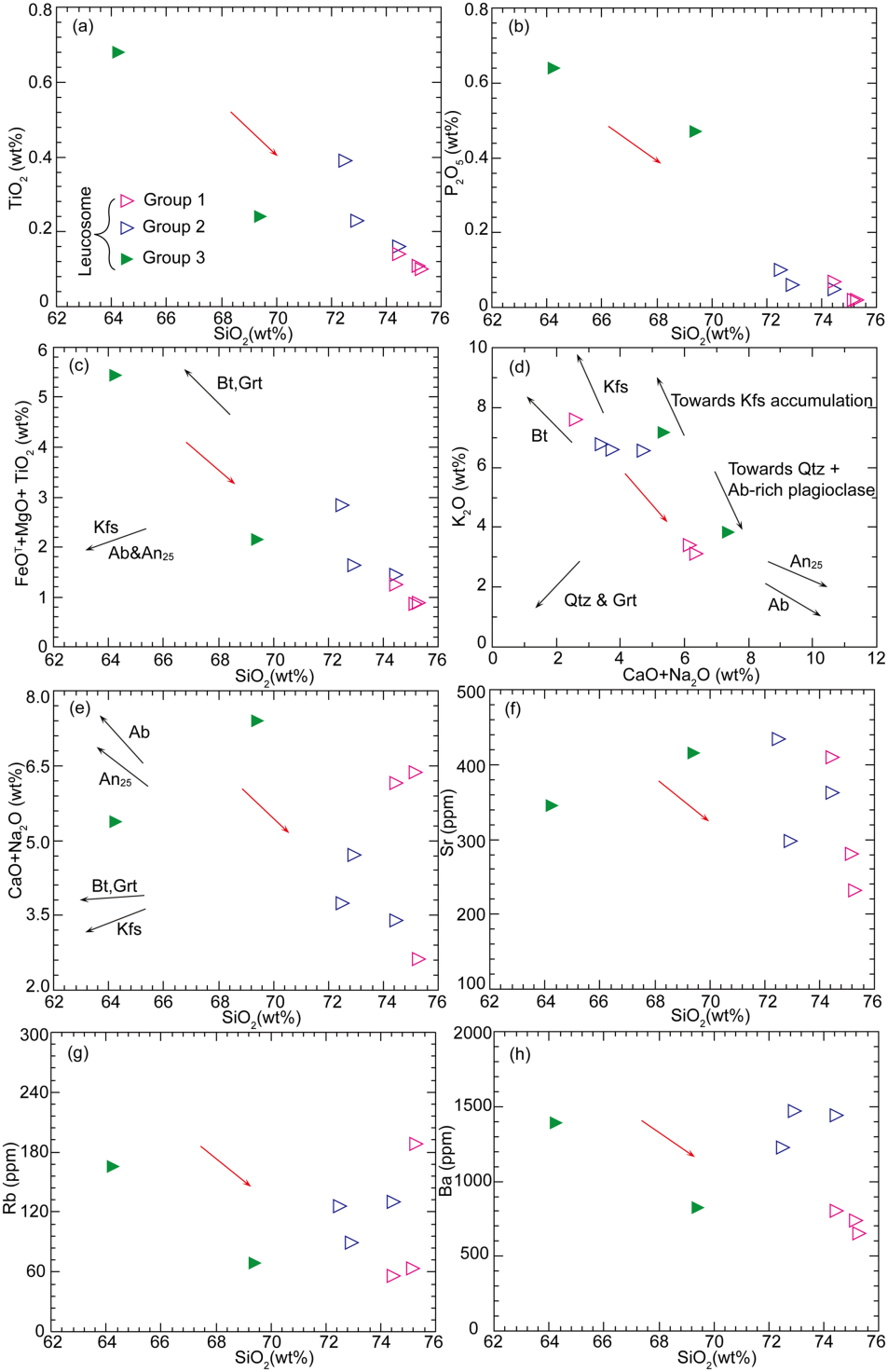
(a)
TiO2 (wt%)
SiO2(wt%)
Leucosome
Group 1
Group 2
Group 3
(b)
P2O5 (wt%)
SiO2(wt%)
(c)
FeOT+MgO+ TiO2 (wt%)
SiO2(wt%)
Bt,Grt
Kfs
Ab&An25
(d)
K2O (wt%)
CaO+Na2O (wt%)
Kfs
Towards Kfs accumulation
Bt
Towards Qtz +
Ab-rich plagioclase
An25
Qtz & Grt
Ab
(e)
CaO+Na2O (wt%)
SiO2(wt%)
Ab
An25
Bt,Grt
Kfs
(f)
Sr (ppm)
SiO2(wt%)
(g)
Rb (ppm)
SiO2(wt%)
(h)
Ba (ppm)
SiO2(wt%)

Figure 6

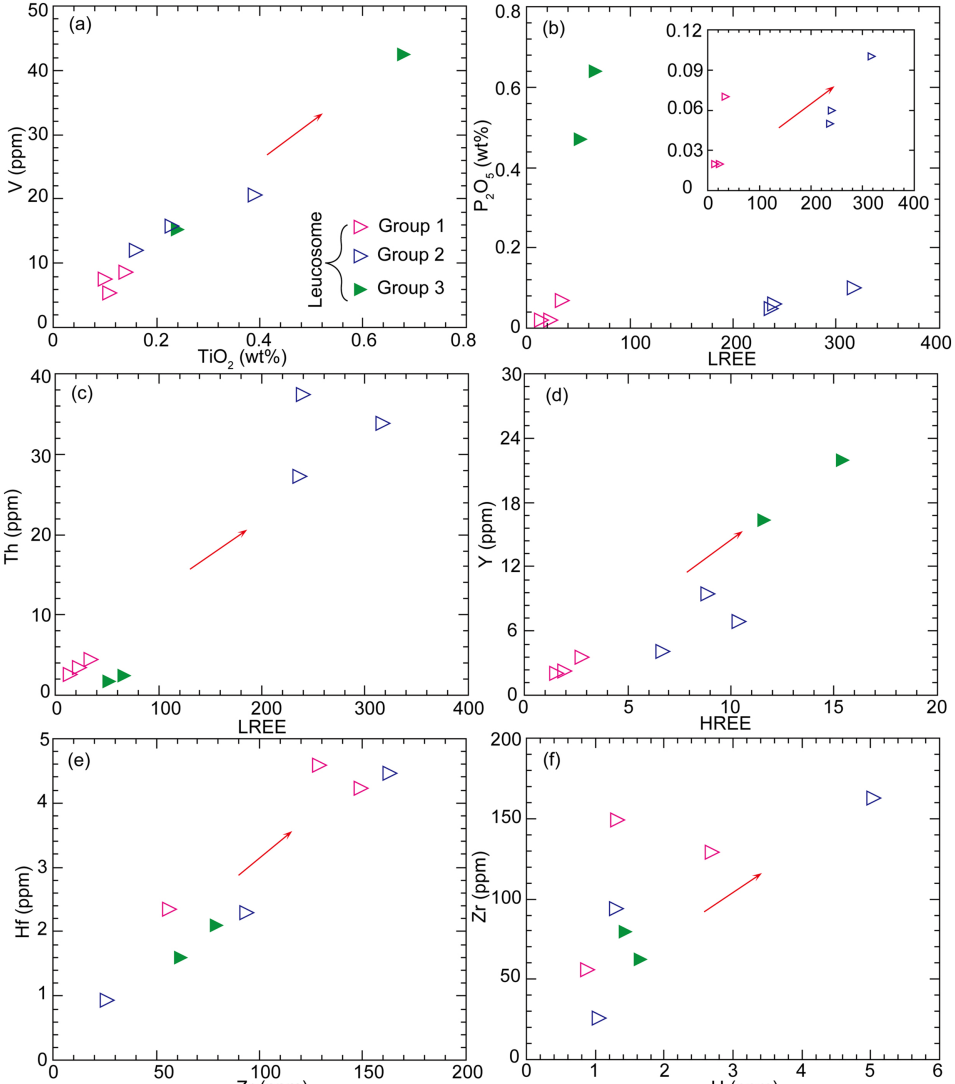
(a)
V (ppm)
TiO2 (wt%)
Leucosome
Group 1
Group 2
Group 3
(b)
P2O5 (wt%)
LREE
(c)
Th (ppm)
LREE
(d)
Y (ppm)
HREE
(e)
Hf (ppm)
Zr (ppm)
(f)
Zr (ppm)
U (ppm)

Figure 7

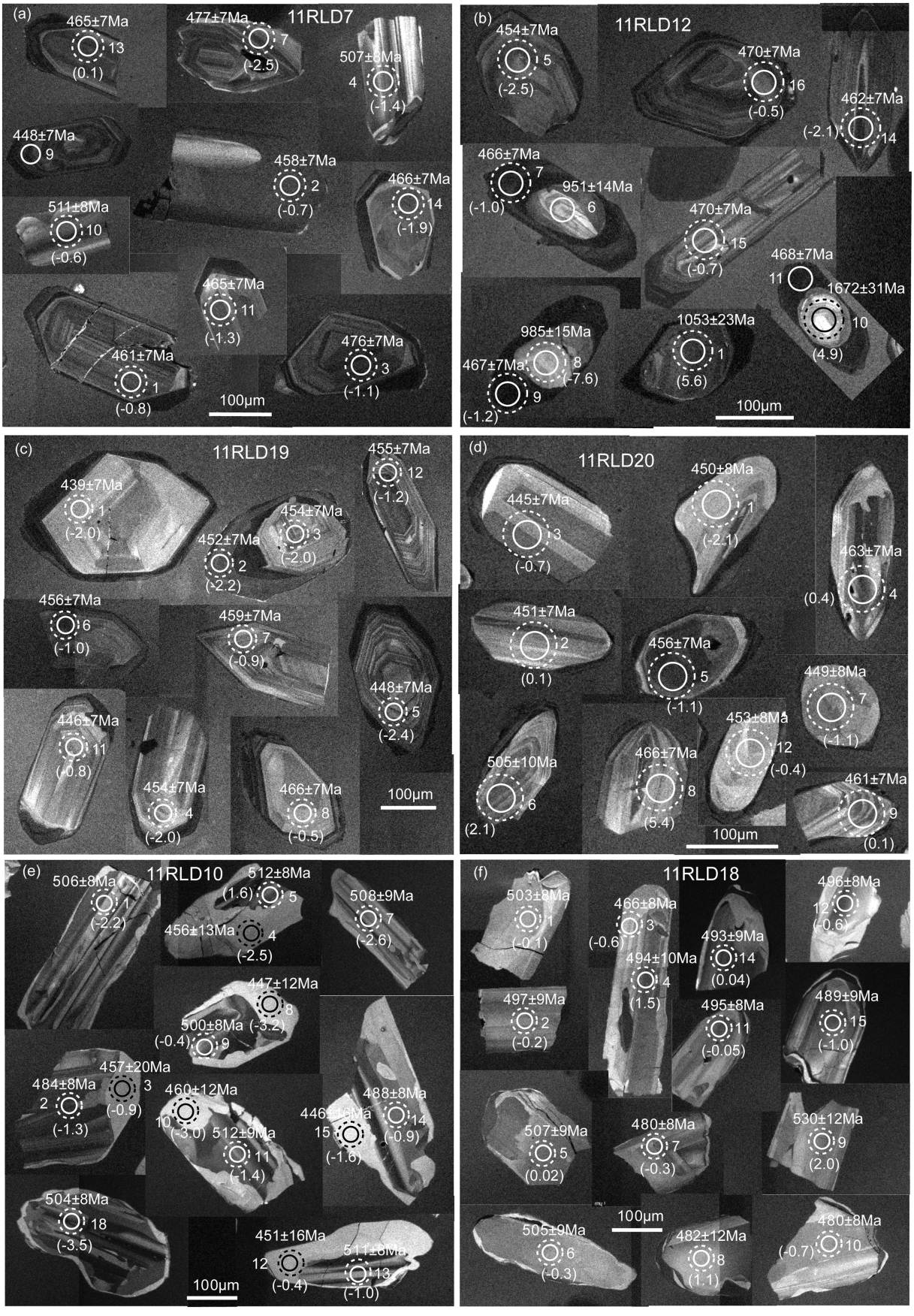
(a)
11RLD7
465±7Ma
13
(0.1)
477±7Ma
7
(-2.5)
507±8Ma
4
(-1.4)
448±7Ma
9
458±7Ma
2
(-0.7)
466±7Ma
14
(-1.9)
511±8Ma
10
(-0.6)
465±7Ma
11
(-1.3)
461±7Ma
1
(-0.8)
476±7Ma
3
(-1.1)
100μm
(b)
11RLD12
454±7Ma
5
(-2.5)
470±7Ma
16
(-0.5)
462±7Ma
14
(-2.1)
466±7Ma
7
(-1.0)
951±14Ma
6
470±7Ma
15
(-0.7)
468±7Ma
11
1672±31Ma
10
(4.9)
985±15Ma
8
(-7.6)
467±7Ma
9
(-1.2)
1053±23Ma
1
(5.6)
100μm
(c)
11RLD19
439±7Ma
1
(-2.0)
455±7Ma
12
(-1.2)
452±7Ma
2
(-2.2)
454±7Ma
3
(-2.0)
456±7Ma
6
(-1.0)
459±7Ma
7
(-0.9)
448±7Ma
5
(-2.4)
446±7Ma
11
(-0.8)
454±7Ma
4
(-2.0)
466±7Ma
8
(-0.5)
100μm
(d)
11RLD20
445±7Ma
3
(-0.7)
450±8Ma
1
(-2.1)
463±7Ma
4
(0.4)
451±7Ma
2
(0.1)
456±7Ma
5
(-1.1)
449±8Ma
7
(-1.1)
505±10Ma
6
(2.1)
466±7Ma
8
(5.4)
453±8Ma
12
(-0.4)
461±7Ma
9
(0.1)
100μm
(e)
11RLD10
506±8Ma
1
(-2.2)
512±8Ma
5
(1.6)
456±13Ma
4
(-2.5)
508±9Ma
7
(-2.6)
447±12Ma
8
(-3.2)
500±8Ma
9
(-0.4)
457±20Ma
3
(-0.9)
484±8Ma
2
(-1.3)
460±12Ma
10
(-3.0)
512±9Ma
11
(-1.4)
488±8Ma
14
(-0.9)
15
(-1.6)
504±8Ma
18
(-3.5)
451±16Ma
12
(-0.4)
511±8Ma
13
(-1.0)
100μm
(f)
11RLD18
503±8Ma
1
(-0.1)
466±8Ma
3
(-0.6)
496±8Ma
12
(-0.6)
493±9Ma
14
(0.04)
494±10Ma
4
(1.5)
497±9Ma
2
(-0.2)
495±8Ma
11
(-0.05)
489±9Ma
15
(-1.0)
507±9Ma
5
(0.02)
480±8Ma
7
(-0.3)
530±12Ma
9
(2.0)
100μm
505±9Ma
6
(-0.3)
482±12Ma
8
(1.1)
480±8Ma
10
(-0.7)

Figure 8

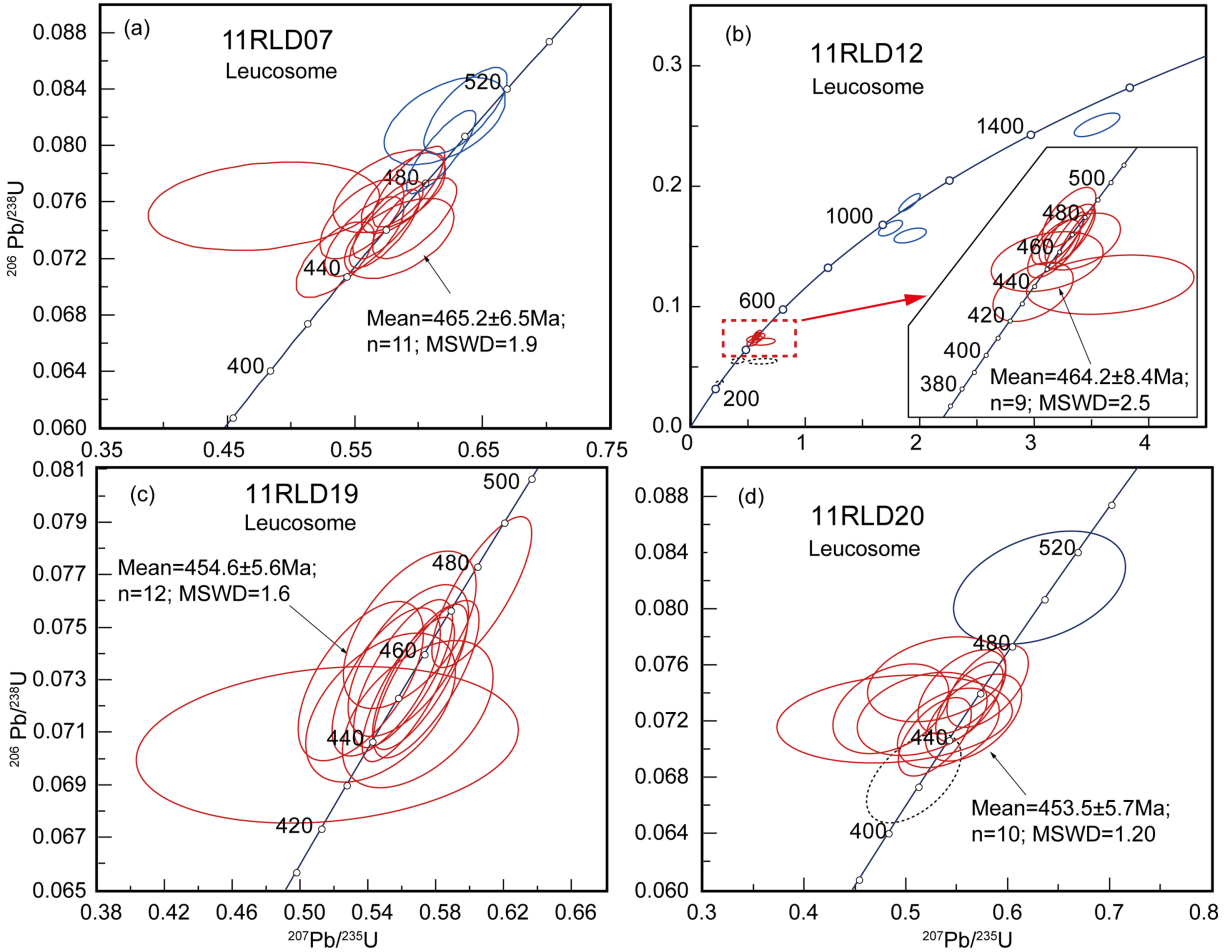
(a)
11RLD07
Leucosome
520
480
440
400
Mean=465.2±6.5Ma;
n=11; MSWD=1.9
(b)
11RLD12
Leucosome
1400
1000
600
200
500
480
460
440
420
400
380
Mean=464.2±8.4Ma;
n=9; MSWD=2.5
(c)
11RLD19
Leucosome
Mean=454.6±5.6Ma;
n=12; MSWD=1.6
500
480
460
440
420
(d)
11RLD20
Leucosome
520
480
440
400
Mean=453.5±5.7Ma;
n=10; MSWD=1.20
206 Pb/238U
207Pb/235U

Figure 9

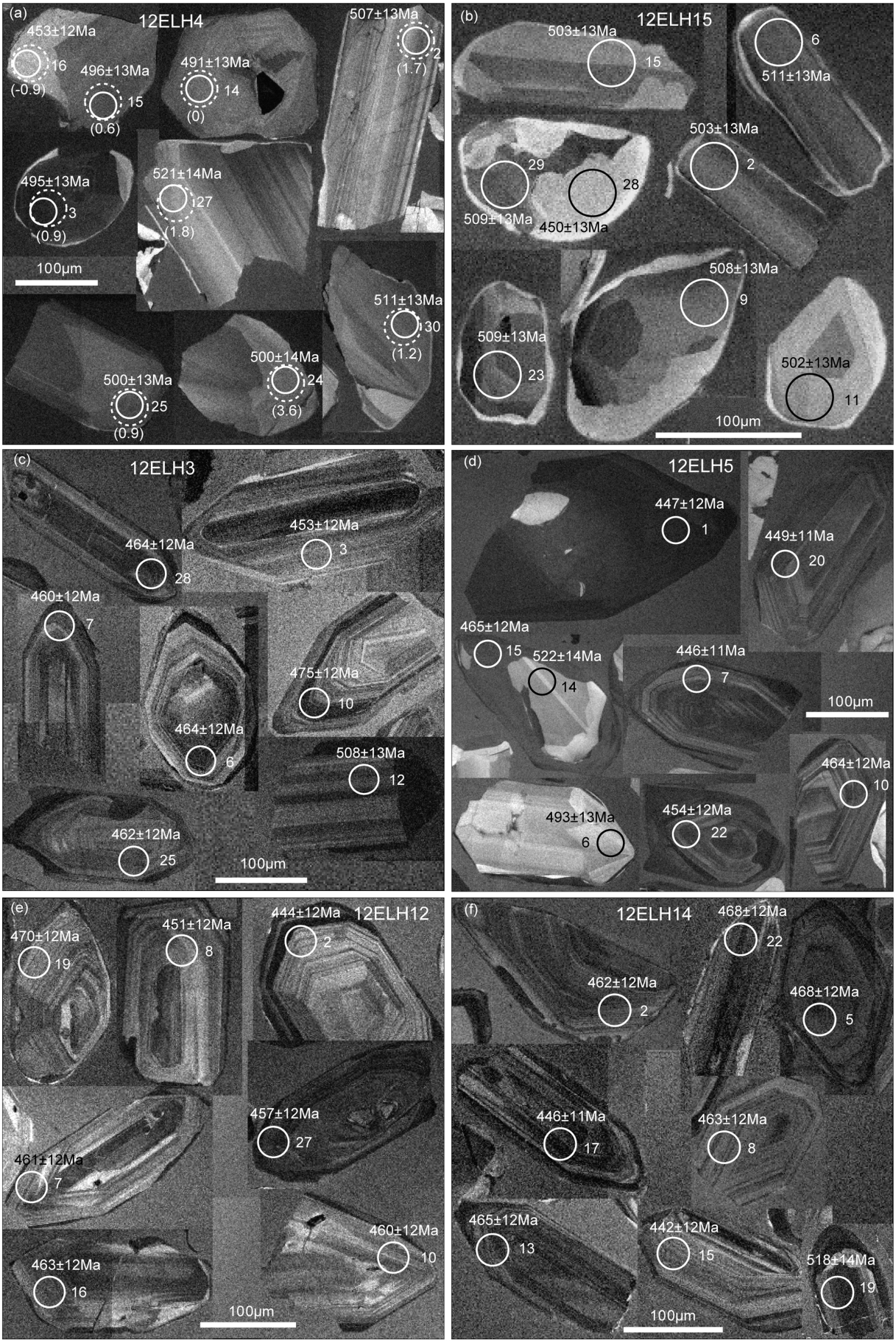
(a)
12ELH4
453±12Ma
16
(-0.9)
496±13Ma
15
(0.6)
491±13Ma
14
(0)
507±13Ma
2
(1.7)
521±14Ma
27
(1.8)
495±13Ma
3
(0.9)
100μm
511±13Ma
30
(1.2)
500±14Ma
24
(3.6)
500±13Ma
25
(0.9)
(b)
12ELH15
503±13Ma
15
6
511±13Ma
503±13Ma
2
29
28
509±13Ma
450±13Ma
508±13Ma
9
509±13Ma
23
502±13Ma
11
100μm
(c)
12ELH3
453±12Ma
3
464±12Ma
28
460±12Ma
7
475±12Ma
10
464±12Ma
6
508±13Ma
12
462±12Ma
25
100μm
(d)
12ELH5
447±12Ma
1
449±11Ma
20
465±12Ma
15
522±14Ma
14
446±11Ma
7
100μm
464±12Ma
10
493±13Ma
6
454±12Ma
22
(e)
12ELH12
470±12Ma
19
451±12Ma
8
444±12Ma
2
457±12Ma
27
461±12Ma
7
460±12Ma
10
463±12Ma
16
100μm
(f)
12ELH14
468±12Ma
22
462±12Ma
2
468±12Ma
5
446±11Ma
17
463±12Ma
8
465±12Ma
13
442±12Ma
15
518±14Ma
19
100μm

Figure 10

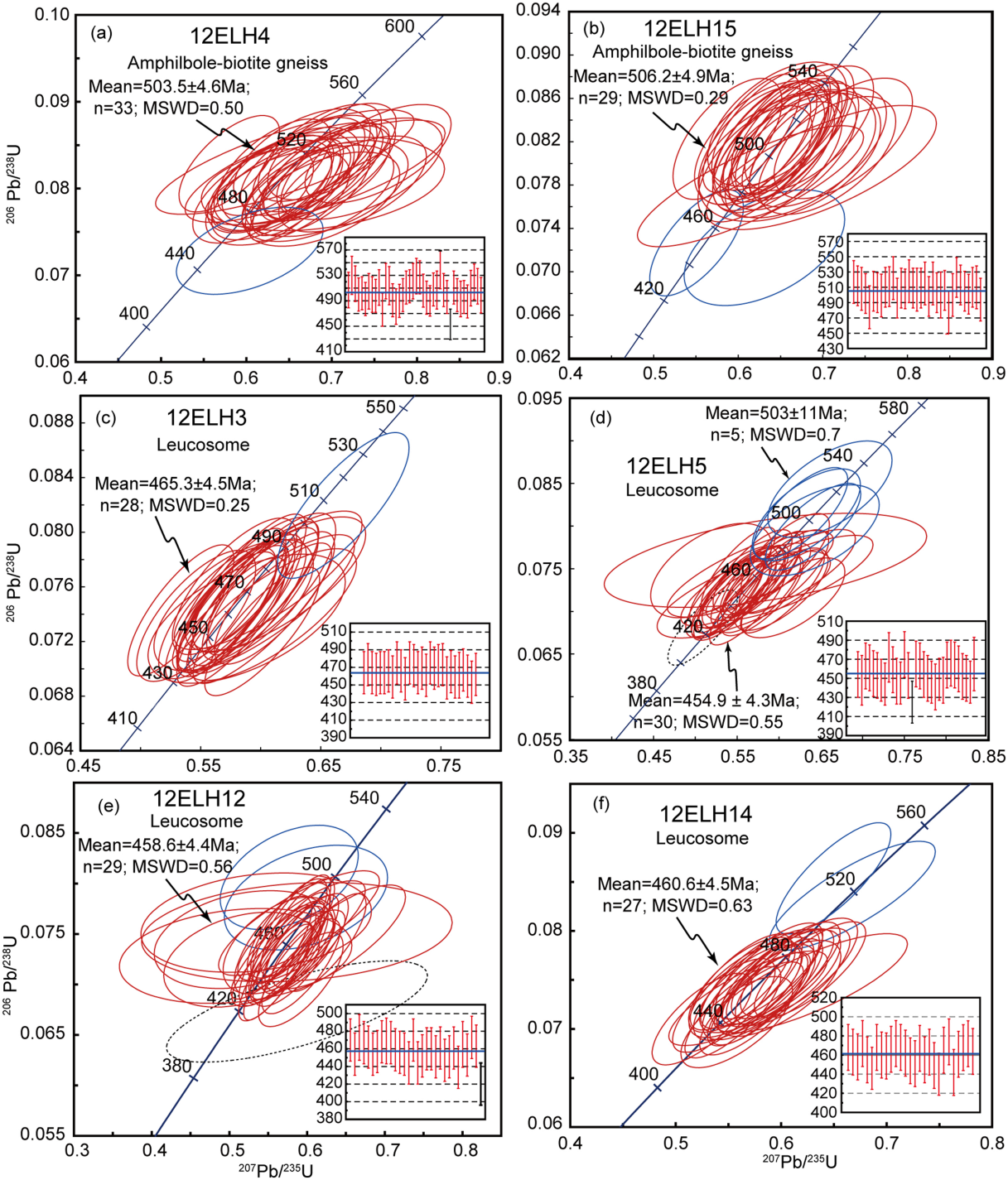
(a)
12ELH4
Amphilbole-biotite gneiss
Mean=503.5±4.6Ma;
n=33; MSWD=0.50
(b)
12ELH15
Amphilbole-biotite gneiss
Mean=506.2±4.9Ma;
n=29; MSWD=0.29
(c)
12ELH3
Leucosome
Mean=465.3±4.5Ma;
n=28; MSWD=0.25
(d)
Mean=503±11Ma;
n=5; MSWD=0.7
12ELH5
Leucosome
380
Mean=454.9 ± 4.3Ma;
n=30; MSWD=0.55
(e)
12ELH12
Leucosome
Mean=458.6±4.4Ma;
n=29; MSWD=0.56
(f)
12ELH14
Leucosome
Mean=460.6±4.5Ma;
n=27; MSWD=0.63
206 Pb/238U
207Pb/235U

Figure 11

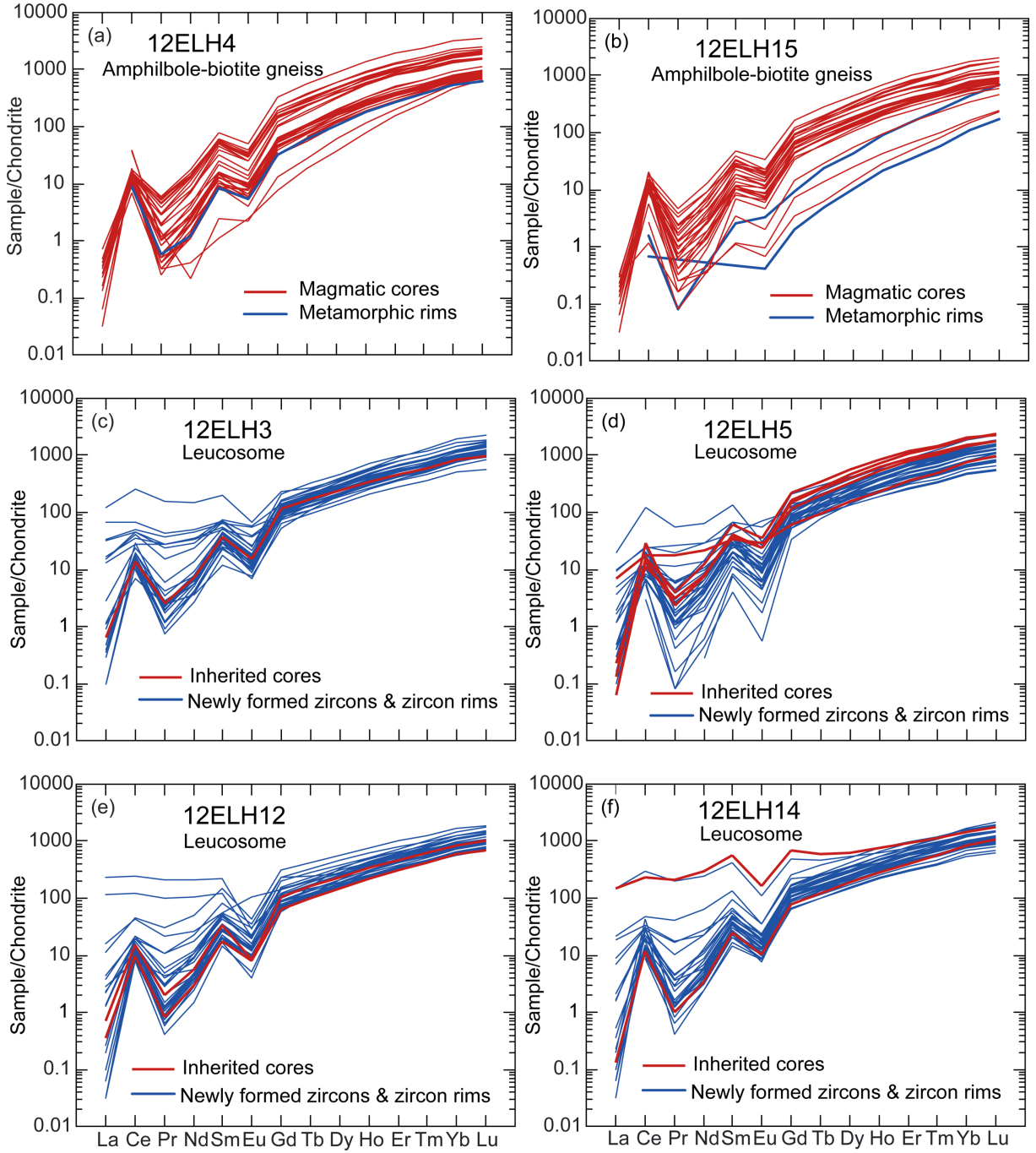
(a)
12ELH4
Amphilbole-biotite gneiss
Magmatic cores
Metamorphic rims
(b)
12ELH15
Amphilbole-biotite gneiss
Magmatic cores
Metamorphic rims
(c)
12ELH3
Leucosome
Inherited cores
Newly formed zircons & zircon rims
(d)
12ELH5
Leucosome
Inherited cores
Newly formed zircons & zircon rims
(e)
12ELH12
Leucosome
Inherited cores
Newly formed zircons & zircon rims
(f)
12ELH14
Leucosome
Inherited cores
Newly formed zircons & zircon rims
Sample/Chondrite
10000
1000
100
10
1
0.1
0.01
La Ce Pr Nd Sm Eu Gd Tb Dy Ho Er Tm Yb Lu

Figure 12

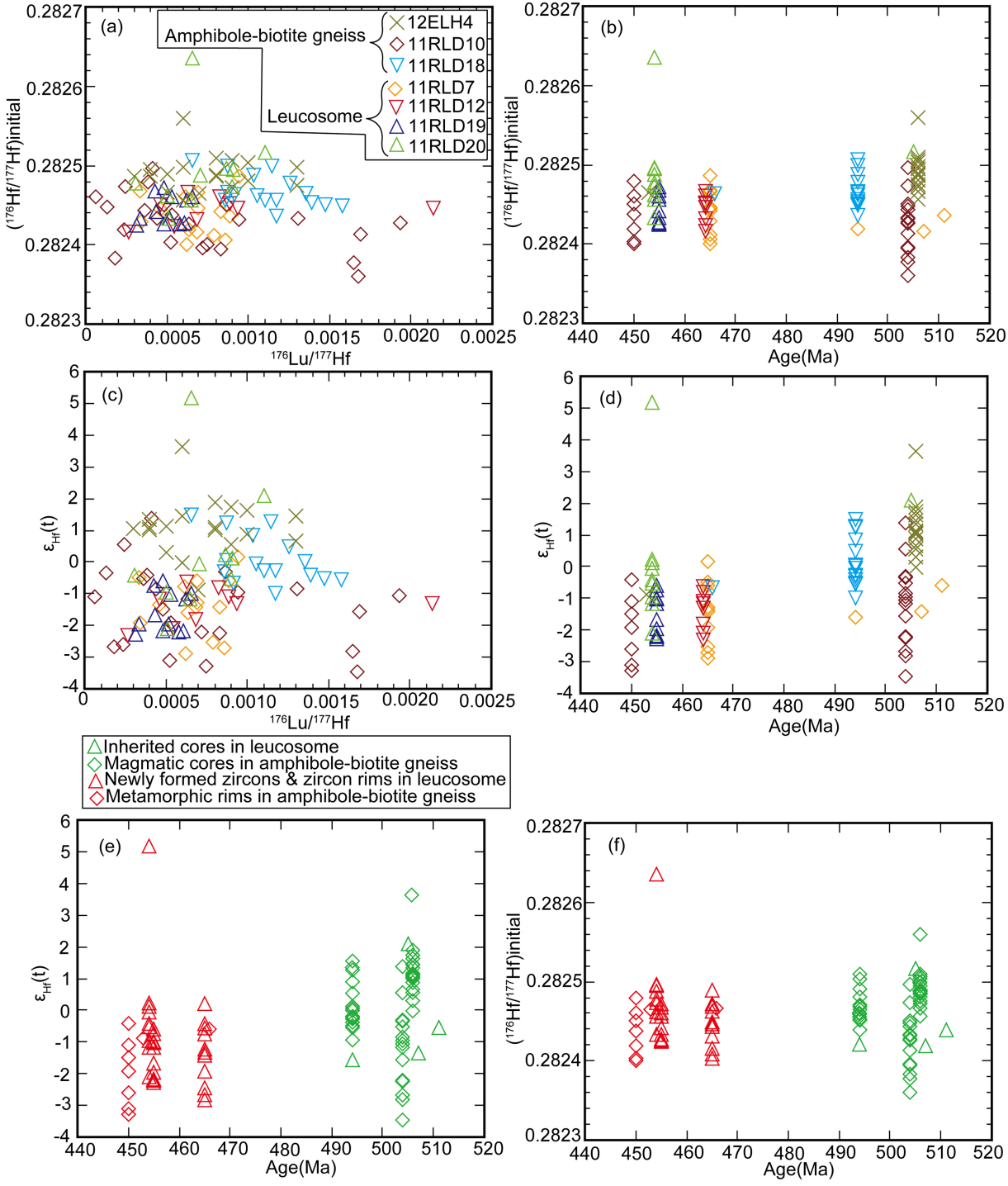
(a)
Amphibole-biotite gneiss
12ELH4
11RLD10
11RLD18
Leucosome
11RLD7
11RLD12
11RLD19
11RLD20
(176Hf/177Hf)initial
176Lu/177Hf
(b)
Age(Ma)
(c)
εHf(t)
(d)
Inherited cores in leucosome
Magmatic cores in amphibole-biotite gneiss
Newly formed zircons & zircon rims in leucosome
Metamorphic rims in amphibole-biotite gneiss
(e)
(f)

Figure 13